

Article

Metabasites from the Central East Kunlun Orogenic Belt Inform a New Suture Model for Subduction and Collision in the Early Paleozoic Proto-Tethys Ocean

Feng Chang, Guibin Zhang *, Lu Xiong, Shuaiqi Liu, Shuzhen Wang and Yixuan Liu

The Key Laboratory of Orogenic Belts and Crustal Evolution, Ministry of Education, School of Earth and Space Sciences, Peking University, Beijing 100871, China; changf@stu.pku.edu.cn (F.C.)

* Correspondence: gbzhang@pku.edu.cn

Abstract: The discovery of eclogite outcrops in the East Kunlun Orogen Belt (EKOB) has confirmed the existence of an Early Paleozoic HP-UHP metamorphic belt. However, the protoliths and metamorphic histories of widespread metabasites remain poorly constrained. We collected three types of metabasites from the central part of EKOB. We present an integrated study of petrography, whole-rock geochemistry, Sr-Nd isotopes, estimated P-T conditions, and zircon U-Pb isotope ages. The results show that amphibolites and retrograde eclogites have clockwise P-T paths with peak conditions of, respectively, 11–12 kbar and 675–695 °C, and 21.5–22.2 kbar and 715–750 °C. Zircon dating of metabasites from Dagele yields Late Ordovician (~449 Ma) to Early Silurian (~440 Ma) protolith ages and Early Devonian (~414 Ma) amphibolite facies metamorphic ages. Retrograde eclogites from east Nuomuhong have a protolith age of ~902 Ma and metamorphic ages of ~418 Ma, consistent with other eclogites from East Kunlun. Our data suggest that the protoliths of Dagele metabasites represent arc-type magmatism during the subduction of a small back-arc oceanic basin. Instead, the protoliths of retrograde eclogites are Neoproterozoic tholeiitic basalts emplaced into continental crust and subsequently deeply subducted. We develop a new model for Early Paleozoic subduction and collision in the East Kunlun region, emphasizing the role of ‘dominant’ and ‘secondary’ suture boundaries. This model helps explain the ages and metamorphic histories of the metabasites studied here and offers new perspectives on the evolution of the Proto-Tethys Ocean.

Keywords: metabasites; protoliths; Proto-Tethys Ocean; dominant-secondary suture; East Kunlun



Citation: Chang, F.; Zhang, G.; Xiong, L.; Liu, S.; Wang, S.; Liu, Y.

Metabasites from the Central East Kunlun Orogenic Belt Inform a New Suture Model for Subduction and Collision in the Early Paleozoic Proto-Tethys Ocean. *Minerals* **2024**, *14*, 449. <https://doi.org/10.3390/min14050449>

Academic Editor: Bernhard Schulz

Received: 31 March 2024

Revised: 18 April 2024

Accepted: 19 April 2024

Published: 24 April 2024



Copyright: © 2024 by the authors. Licensee MDPI, Basel, Switzerland. This article is an open access article distributed under the terms and conditions of the Creative Commons Attribution (CC BY) license (<https://creativecommons.org/licenses/by/4.0/>).

1. Introduction

Studying the nature of magmatism and metamorphism at different stages of the Wilson cycle can provide valuable insights into regional tectonics and deep Earth processes. In particular, analysis of different types of metabasites deformed across a range of metamorphic facies (mainly greenschist, amphibolite, eclogite, and granulite) has proven significant in understanding the role of subduction- and collision-related processes in the context of regional tectonics [1].

The East Kunlun Orogenic Belt (EKOB) in northwest China (Figure 1) crosses the Proto-Tethys and Paleo-Tethys domains, corresponding to two Wilson cycles. Paleozoic ophiolites and related metamorphic units in the EKOB preserve a valuable record of the geodynamics of the northern Gondwana margin during the evolution of the Proto-Tethys Ocean [2]. Over the past decade, ophiolitic mélanges [3–6] and eclogites in the EKOB [7–12] have been targets for petrological and geochemical studies focused on understanding metamorphic histories and P–T paths. Results show that these metabasites record diverse Early Paleozoic high- to ultrahigh-pressure (HP-UHP) metamorphic conditions and thus provide an opportunity to understand the transition from subduction to continental collision within the Proto-Tethys domain [8–10,13].

Although eclogites within the EKOB have received much attention, amphibolites' distribution and geological history are poorly understood. Some studies suggest that the amphibolites are eclogite's retrogressed equivalents, while others favor a P–T history involving peak amphibolite facies metamorphism (e.g., [14,15]). Better resolving the metamorphic conditions and P–T paths of the amphibolites and eclogites, as well as the formation settings of the Early Paleozoic ophiolites, will result in a clearer picture of the tectonic history in East Kunlun, especially the evolution of the trench-arc-back arc system that was active in the Proto-Tethyan Ocean.

In this study, we focus on several newly collected amphibolite and eclogite samples from the Dagele and east Nuomuhong areas (Figure 1). The Dagele Ophiolite has been identified as a supra-subduction zone ophiolite (SSZ ophiolite) mainly composed of serpentinized dunite, gabbro, and eclogite [12]. Using petrological and geochemical analyses, phase equilibrium modeling, and trace element geothermometry, we quantitatively constrain our samples' P–T path, petrogenesis, and formation ages. Based on this and building on previous studies, we interpret the possible Early Paleozoic tectonic histories of the metabasites within the context of the EKOB.

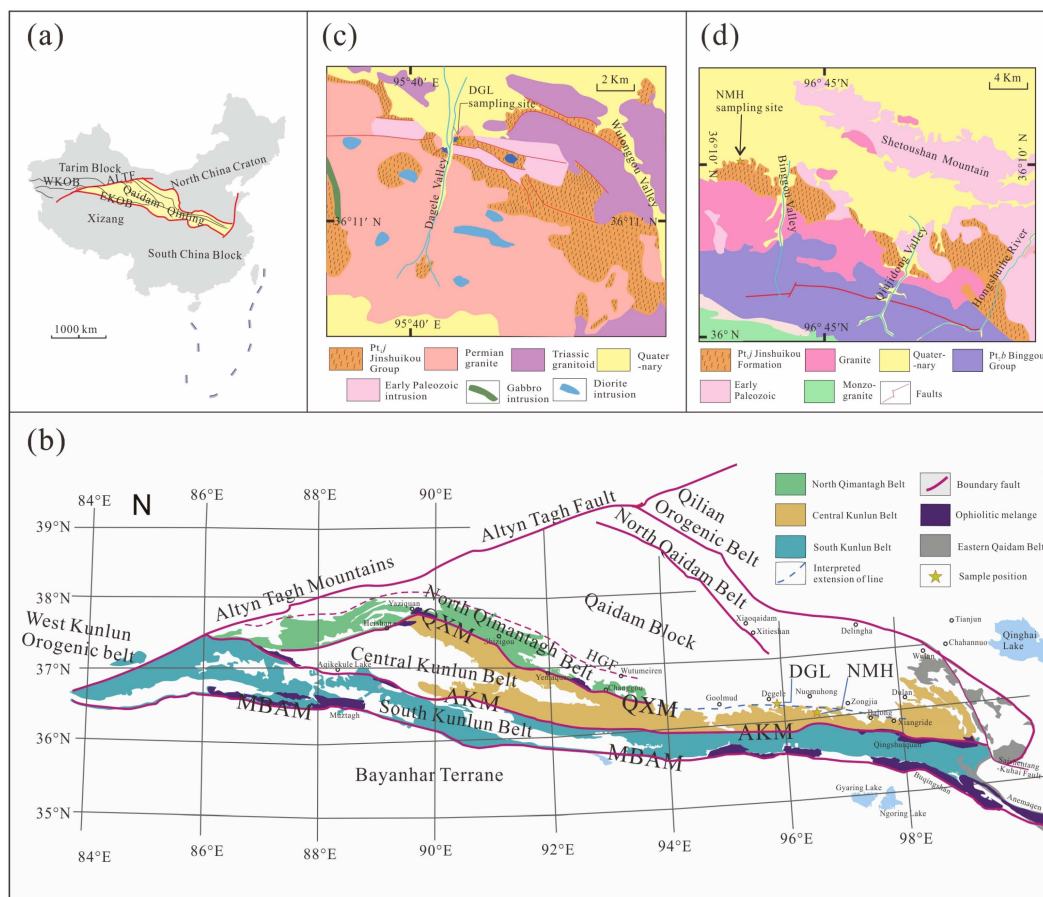


Figure 1. Geological and tectonic setting. (a) Overview map showing the location of Kunlun within the Chinese Central Orogenic Belt (modified from Dong et al. [16]). (b) A simplified tectonic map of Kunlun showing major tectonic divisions, ophiolitic mélanges, and sampling locations (modified from Dong et al. [16]). HGF—Hongliuquan–Golmud Fault; QXM—Qimantag–Xiangride ophiolitic mélange; AKM—Aqikekulehu–Kunzhong ophiolitic mélange; MBAM—Muztag–Buqingshan–Animaqen ophiolitic mélange; DGL—Dagele area shown in part (c); NMH—Nuomuhong area shown in part (d). (c) Geological map and sampling site in Dagele (modified from Feng et al. [17] and Li et al. [18]); (d) Geological map and sampling site in east Nuomuhong (modified from He et al. [19]).

2. Geological Setting

2.1. Regional Geology and Tectonics

The ~2500 km-long East Kunlun Orogenic Belt (EKOB) lies along the northern margin of the Qinghai–Tibet Plateau and forms the western portion of the Qinling–Qilian–Kunlun orogenic lineage. The EKOB is separated from the West Kunlun Orogenic Belt (WKOB) by the sinistral strike-slip Altyn Tagh Fault (ALTF) and from west Qinling by the SaiShentang–Kuhai faults (Figure 1a,b).

The EKOB experienced long-lived subduction and accretionary processes from the Proterozoic to the Triassic, forming an integral part of the Tibetan collisional orogen. The belt was affected by four primary tectono-magmatic cycles of the Precambrian, Early Paleozoic, Late Paleozoic to Early Mesozoic, and Late Mesozoic–Cenozoic [20]. These cycles were associated with the formation and growth of the continent crust in the EKOB, which therefore preserves evidence of processes that took place in the Proto-Tethys and Paleo-Tethys regions. The tectonic framework in this region consists of several major east-west-striking fault zones, which subdivided the EKOB into several terranes. In the past, the East Kunlun Orogenic Belt distributed between Qaidam Block and BayanHar Block was mainly divided into two terranes, North Kunlun Terrane and South Kunlun Terrane, by the Central East Kunlun Fault. While the new architecture is that the Qimantagh–Xiangride mélange zone (QXM), the Aqikekulehu–Kunzhong mélange zone (AKM) divided the orogenic belt as three parts of the North Qimantagh Belt, the Central Kunlun Belt, and the South Kunlun Belt, respectively (Figure 1b, [16]).

2.2. Local Geology and Sampling

The Dagele and east Nuomuhong are located in the central part of the EKOB (Figure 1b–d). Dagele contains an ophiolitic sequence with serpentinized dunite, gabbro, and meter-scale eclogite lenses partially retrogressed to amphibolite. The country rock is gneiss of the Baishahe Formation in the Paleoproterozoic Jinshuikou Group (Figure 2a–c), has a coarse- to medium-grained granoblastic texture and contains biotite, plagioclase, quartz, and minor muscovite. Abundant granodiorites and granites south of the study area yield the Permian–Triassic ages [17,18,20]. We collected two types of metabasite from the Dagele River valley (36°14′38″ N, 95°42′56″ E; Figure 1c): garnet amphibolite and amphibolite (Figure 2a–c).

For the east Nuomuhong (36°11′2″ N, 96°38′59″ E), it is dominated by granitic gneiss, eclogite, and amphibolite, with minor granitoid intrusions (Figure 1d). Metabasites (eclogite or amphibolite) occur as lenses or blocks enclosed in the gneiss of the Paleoproterozoic Jinshuikou Group (Figures 1d and 2d–f). The gneiss has a granoblastic texture and consists of plagioclase, potassium feldspar, quartz, and biotite, with minor garnet (Figure 2g). The metabasite samples from east Nuomuhong preserve evidence of high-pressure metamorphism and are therefore classified as retrograde eclogites.

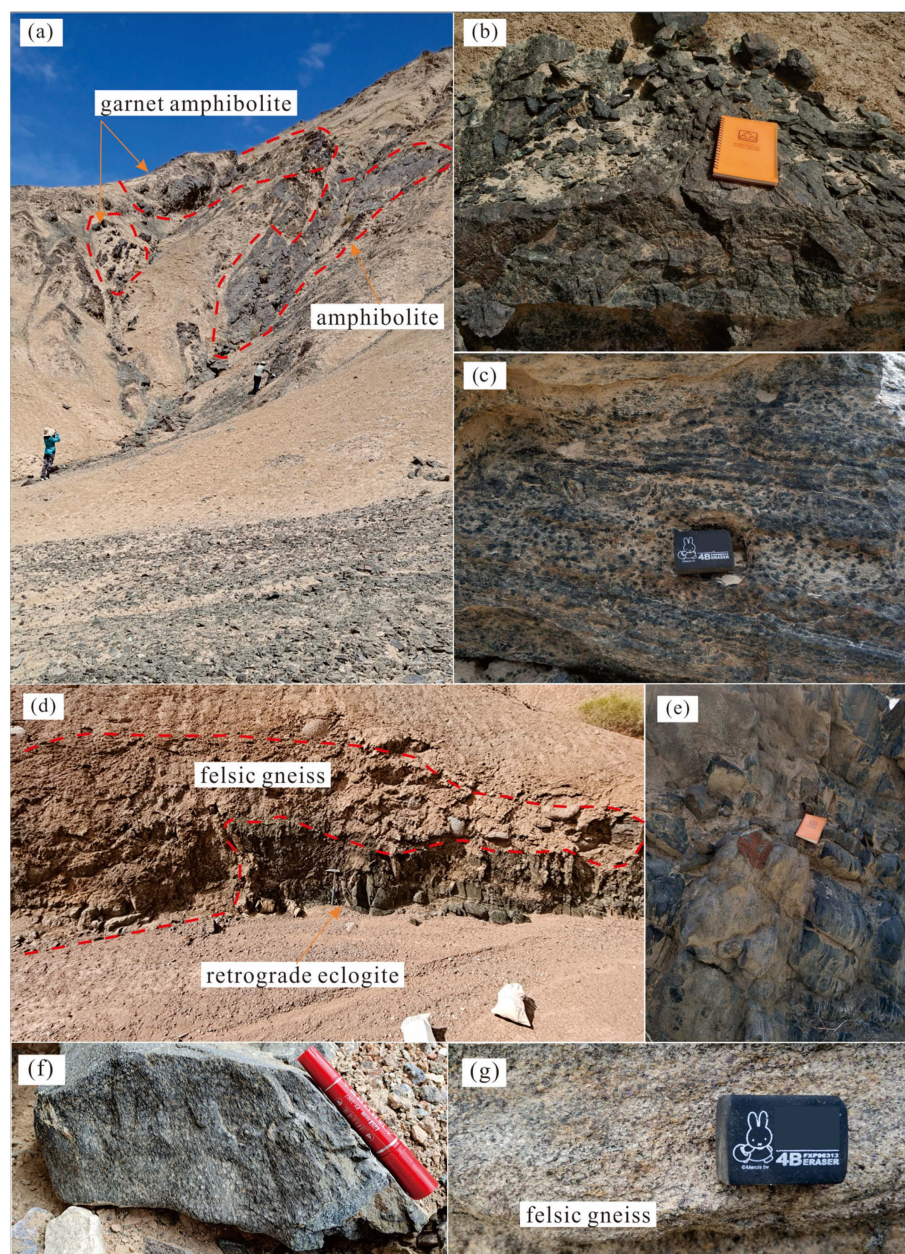


Figure 2. Photographs of metabasites from Dagele (a–c) and east Nuomuhong (d–f). (a) Garnet amphibolite and amphibolite are xenoliths within the host gneiss. (b) Typical amphibolite. (c) Porphyroblastic texture on a weathered surface of garnet amphibolite. (d) Retrograde eclogite within felsic gneiss. (e,f) Typical retrograde eclogite. (g) Granoblastic texture on a fresh surface of felsic gneiss.

3. Analytical Methods

Detailed descriptions of the analytical methods are presented in Supplementary Test S1. Data for electron microprobe analysis (EMPA) compositions of garnet, pyroxene, amphibole, and plagioclase in metabasites are listed in, respectively, Tables S1–S4. Whole-rock major and trace element geochemistry analysis determined by -Fluorescence (XRF) and inductively-coupled plasma mass spectrometer (ICP-MS) are presented in Table S5. Whole-rock Sr-Nd isotopes measured by multicollector (MC) ICP-MS are listed in Table S6. Zircon U–Pb ages ($33\ \mu\text{m} + 10\ \mu\text{m}$ spot sizes) and trace elements ($32\ \mu\text{m}$ spot size) analyzed by laser ablation (LA) MC-ICP-MS are listed in Tables S7–S9.

4. Results

4.1. Petrology of Metabasites

4.1.1. Garnet Amphibolite from Dagele (20DGL97)

Garnet amphibolites are grey-green to dark green and have a porphyroblastic texture (Figure 2c) predominantly consisting of garnet (~20%; Grt), amphibole (~38%; Amp), plagioclase (~26%; Pl), quartz (~10%; Qtz), and accessory rutile (Rt), ilmenite (Ilm), titanite (Ti), and zircon (Zr; Figure 3a–c).

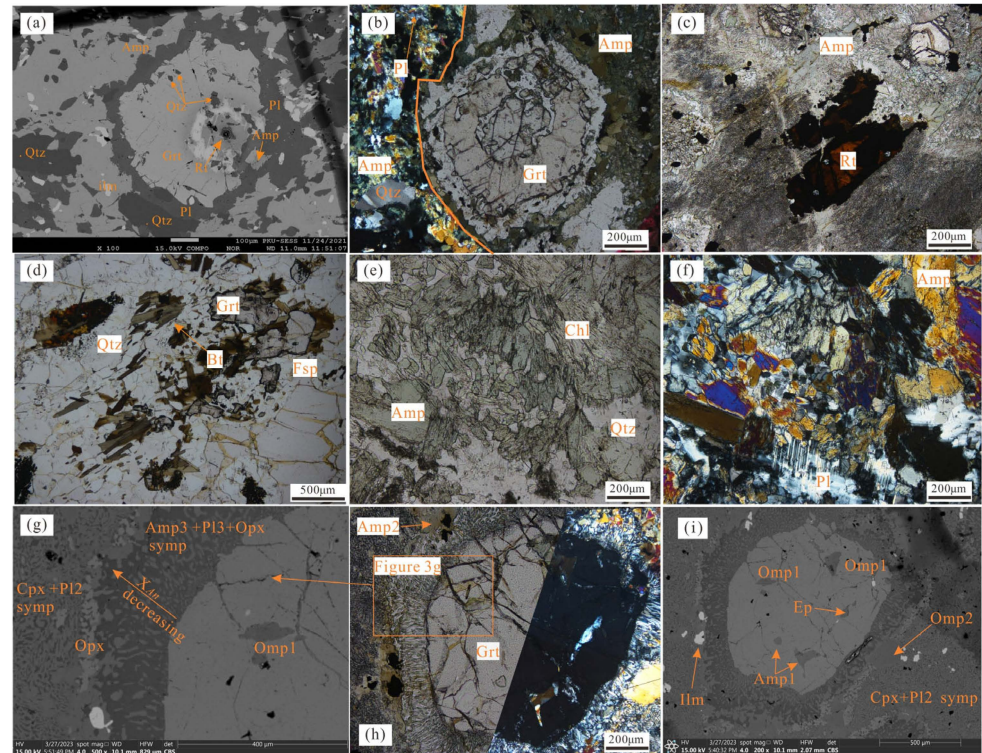


Figure 3. Petrology of metabasites. (a) SEM-backscatter image (SEM-BSE) and (b) photomicrograph of garnet porphyroblast in the matrix of amphibole, plagioclase, quartz, and rutile in garnet amphibolite (20DGL97). Part b combines crossed- and plane-polarized light. (c) Photomicrograph of matrix rutile showing partial replacement by ilmenite (20DGL97). (d) Photomicrograph of felsic gneiss composed of quartz, feldspar, garnet, and biotite. Photomicrographs in plane-polarized (e) and crossed-polarized (f) light of amphibolites composed of amphibole with minor chlorite and plagioclase. (g) SEM-BSE image of retrograde eclogite (20NMH81) showing transition from clinopyroxene + plagioclase2 symplectite to the corona of orthopyroxene + plagioclase3 + amphibole3. Combined crossed- and plane-polarized light photomicrograph (h) and SEM-BSE image (i) of garnet porphyroblast in retrograde eclogite with inclusions of amphibole (Amp1) and epidote, surrounded by a matrix of omphacite2 and clinopyroxene + P12 symplectite (20NMH81).

Garnet porphyroblasts occur as subhedral to euhedral grains (0.2–0.5 mm) exhibiting compositional zoning (core, mantle, and rim zones) and containing abundant quartz, amphibole, and rutile inclusions (Figure 3a,b). The garnet is mainly almandine and grossular (Figure 4a). Garnet is commonly resorbed along grain boundaries with partial replacement by Amp + Pl + Qtz. Compositionally, garnet grains are characterized by a systematic decrease of X_{Grs} [$Ca/(Ca + Mg + Fe + Mn)$] and X_{Sps} [$Mn/(Ca + Mg + Fe + Mn)$] from core to the rim (0.43 to 0.34 and 0.058 to <0.01, respectively), whereas X_{Alm} [$Fe/(Ca + Mg + Fe + Mn)$] and X_{Prp} [$Mg/(Ca + Mg + Fe + Mn)$] increase from core to rim (0.51 to 0.61 and <0.01 to 0.03, respectively) (Figure 4b). However, the edge of garnet grains may show a slight reversal in these overall trends (X_{Alm} and X_{Grs}) in Figure 4b.

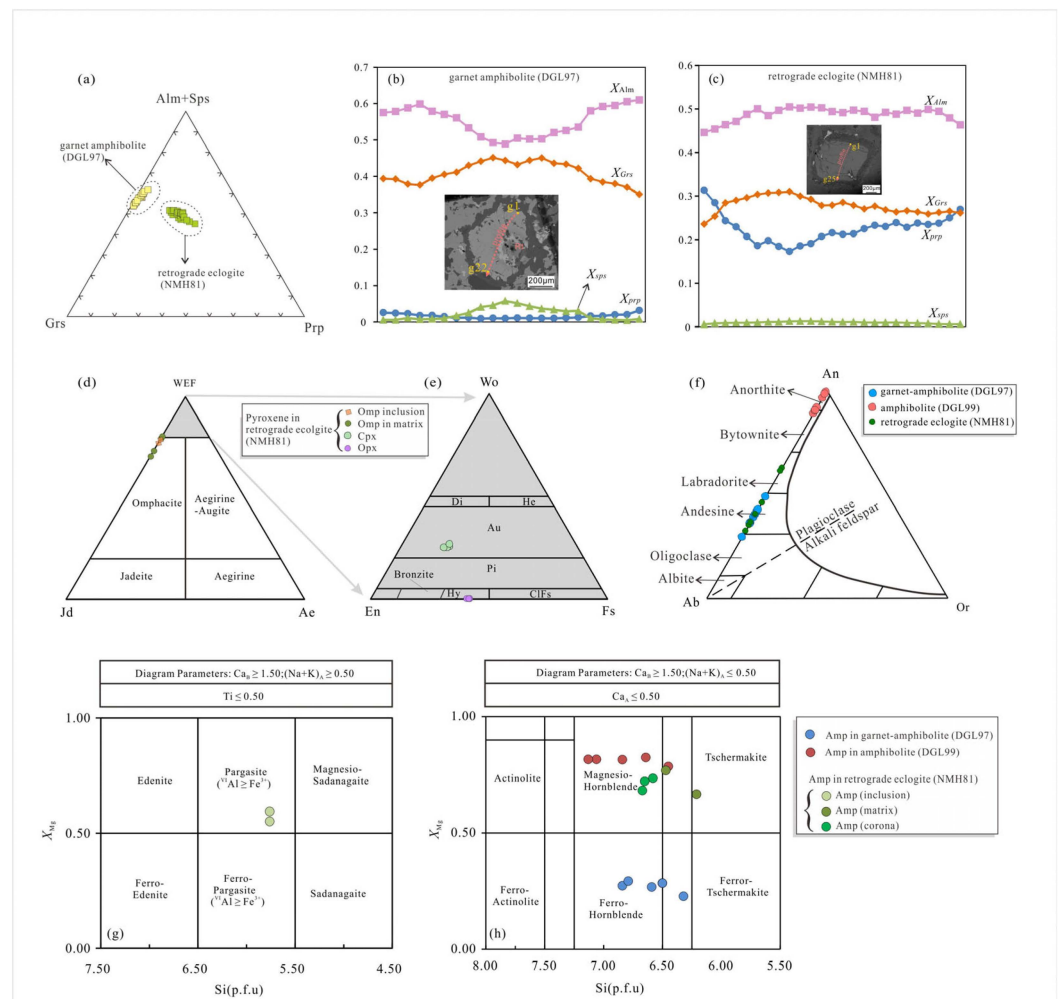


Figure 4. (a) Triangular diagram summarizing garnet compositions. (b,c) Compositional data show profiles across garnet porphyroblasts in garnet amphibolite (DGL97) and retrograde eclogite (NMH81), respectively. $X_{Fe} = Fe^{2+} / (Fe^{2+} + Mn + Mg + Ca)$. X_{Ca} , X_{Mg} and X_{Mn} are defined accordingly. (d,e) Ternary classification diagrams for pyroxene in retrograde eclogite after [21,22] (f) An-Ab-Or triangular diagram [23] showing compositions of plagioclase in retrograde eclogite, garnet amphibolite, and amphibolite (DGL99); (g,h) Compositional variations in amphiboles on plots of $Mg / (Mg + Fe^{2+})$ vs. Si, after [18].

Plagioclase has a subhedral granular texture and occurs in the matrix as anhedral grains and in coronas together with amphibole (Figure 3a), where it has a dominant andesine composition ($X_{An} = 0.36\text{--}0.49$; Figure 4f).

Amphibole occurs as inclusions in garnet, as subhedral matrix grains, and in coronas together with plagioclase (Figure 3b). In all cases the amphibole is classified as ferro-hornblende with $X_{Mg} [=Mg / (Mg + Fe^{2+})] = 0.23\text{--}0.29$ and $(Na + K)_A \leq 0.50$ (per formula unit = p.f.u.) (Figure 4h).

Rutile occurs as anhedral grains in the matrix or as inclusions in garnet. Matrix rutile is partially replaced by ilmenite (Figure 3c) and has a higher zirconium concentration (368–442 ppm) than rutile inclusions in garnet (221–368 ppm).

4.1.2. Amphibolite from Dagele (20DGL99)

Amphibolites are dark grey to black (Figure 2b) and have a granoblastic texture comprising amphibole, plagioclase, chlorite, and accessory minerals (rutile, ilmenite, zircon; Figure 3e,f). Idiomorphic columnar amphibole grains have a composition of $X_{Mg} [=Mg / (Mg + Fe^{2+})] = 0.78\text{--}0.82$ and $(Na + K)_A \leq 0.50$ (p.f.u.), classifying them as

magnesio-hornblende ([24], Figure 4h). Anhedral plagioclase, chlorite, and quartz are found in the interstices of amphibole grains (Figure 3e). Plagioclase has $X_{An} > 0.9$ and can be classified as anorthite (Figure 4f).

4.1.3. Retrograde Eclogite from East Nuomuhong (20NMH81)

Grey-green retrograde eclogites have a porphyroblastic texture consisting of garnet (25%–30%), clinopyroxene (17%–20%, including omphacite), amphibole (15%–20%), plagioclase (30%–35%), minor orthopyroxene (3%–5%), and accessory epidote, rutile, zircon, and ilmenite (Figure 3g–i).

Garnet grains (<0.2 mm) are subhedral to euhedral and contain abundant inclusions of omphacite, amphibole, rutile, and epidote (Figure 3g–i). Garnet shows a slight decrease of X_{Grs} (0.31 to 0.235) and X_{Alm} (0.5 to 0.45) from core to rim, whereas X_{Prp} increases from core (0.17) to rim (0.31; Figure 4c). The edges of grains are replaced by the symplectite assemblage clinopyroxene + plagioclase + amphibole + orthopyroxene + ilmenite (Figure 3g).

Omphacite occurs as well-preserved inclusions in garnet (Omp_1) and as relict matrix grains (Omp_2 ; Figure 3g,i) replaced by the symplectite assemblage of clinopyroxene + plagioclase. The matrix grains have a wider range of jadeite components (19.7–29.6 mol%) compared to omphacite inclusions (21.3–23 mol%; Figure 4d).

Clinopyroxene (Cpx) occurs as a product of omphacite retrogression in the matrix and within coronas around garnet (Figure 3g,i). Matrix Cpx has a relatively high jadeite content (12.5–15 mol%) compared to Cpx in coronas (9.7–11.2 mol%) and is classified as augite (Figure 4e; Table S2).

Amphibole occurs as inclusions in garnet (Amp_1), in the matrix (Amp_2), and within corona symplectites (Amp_3) around garnet (Figure 3h,i). Inclusions are pargasite and have lower Si contents (5.76 p.f.u.), X_{Mg} (0.55–0.59), and Ti contents (=0.04 p.f.u.), and higher Al^{IV} contents (=2.24 p.f.u.) than amphibole in the matrix and in coronas (Figure 4g; Table S3). Matrix and corona amphibole are dominated by magnesio-hornblende compositions with X_{Mg} of 0.66–0.77 (Figure 4h).

Plagioclase occurs as inclusions in matrix omphacite (Pl_1), as symplectite in the matrix (Pl_2), and within coronas around garnet (Pl_3) (Figure 3g). Pl_1 and Pl_2 have a narrower range of X_{An} (0.33 and 0.41–0.47, respectively) than Pl_3 (X_{An} 0.36–0.64). In Pl_3 plagioclase, X_{An} decreases systematically towards the outer edge of the coronas (Figures 3g and 4f; Table S4).

Orthopyroxene with X_{En} of 0.57–0.59 (hypersthene; Figure 4e and Table S2) primarily occurs in corona symplectites in association with Pl_3 and Amp_3 (Figure 3g). Rutile and epidote occur as inclusions within garnet and as small grains in the matrix (Figure 3i).

In the retrograde eclogite, four similar stages of metamorphic mineral assemblage can be identified: (1) Grt core + Amp_1 + Ep + Omp_1 + Rt (as inclusions within garnet) (M I), (2) Grt rim + relict grains of Omp_2 + Rt (M II), (3) Cpx + Pl_{1-2} + Amp_2 + Ilm (M III), and (4) Opx + Pl_3 + Amp_3 + Pl_3 + Ilm surrounding the garnet (M IV).

4.2. Whole-Rock Compositions and Protoliths

All but one sample from Dagele ($n = 18$) and east Nuomuhong ($n = 15$) has a loss of ignition (LOI) values of <2 wt% (Table S5), reflecting the overall low degree of alteration of the metabasites. The east Nuomuhong samples have lower LOI values (0.15–1.53, average: 0.67 wt%) than Dagele (0.07–2.82, average: 1.38 wt%), consistent with the lithologic distinctions described previously. Some samples with relatively high LOI values (e.g., 20NMH82, 20DGL100, and 20DGL105) suggest that secondary hydrated and carbonated phases may be present.

4.2.1. Dagele (DGL) Metabasites

Metabasites from Dagele have SiO_2 of 41.62–53.38 wt.% and TiO_2 of 0.01–5.27 wt.%. They are low-K and sub-alkaline in composition with slight variations in alkalis (1.33–2.45 wt.%)

and notable variations in both $Mg^\#$ (19.58–79.86) and Al_2O_3 contents (10.65–22.70 wt.%). The samples plot mainly in the basalt field on diagrams of SiO_2 vs. $Na_2O + K_2O$ and Zr/Ti vs. Nb/Y (Figure 5a,b, [25,26]). Sub-alkaline samples fall into the tholeiitic basalt field on a FeO^T -($Na_2O + K_2O$)- MgO plot and the island arc tholeiite field on a Co - Th diagram ([27–29]; Figure 5c,d).

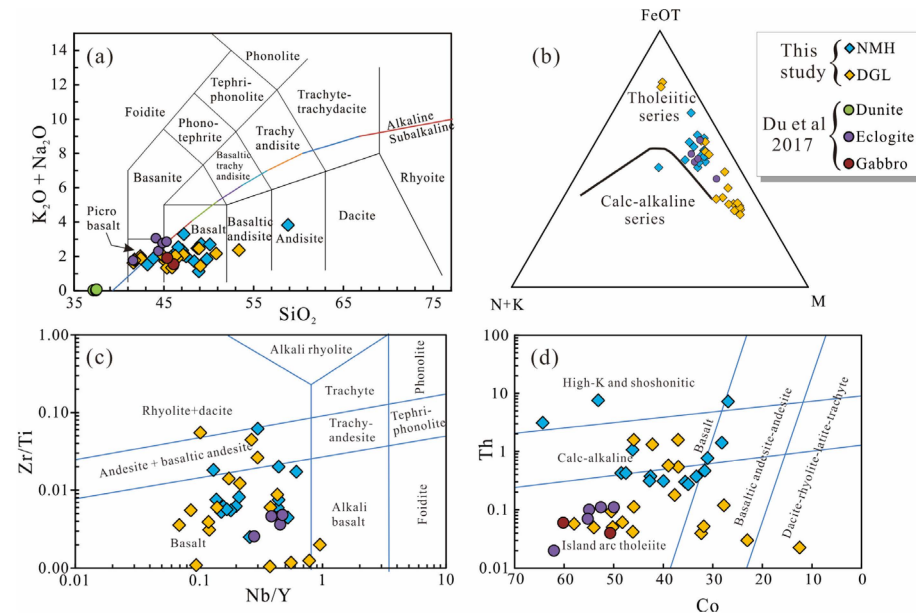


Figure 5. Classification of studied metabasites. (a) Classification of volcanic rocks based on total alkalis ($K_2O + Na_2O$) vs. SiO_2 . (b) AFM diagram for metabasites. (c) Nb/Y vs. Zr/Ti for metabasites. (d) Th vs. Co diagram to determine the protoliths of metabasites (Hastie et al. [29]).

Garnet amphibolites (20DGL97, 98) contain total REE contents of 104–129 ppm, HREE contents of 72–94 ppm, and LREE contents of 32–36 ppm. Chondrite-normalized REE patterns are sub-parallel and show negative Eu anomalies (close to 0.8) and slight enrichment in LREE relative to HREE ($(La/Yb)_N$ of 1.40–1.98). This places the garnet amphibolites above the literature values for E-MORB [30] and gabbro from [12] (Figure 6a). In contrast, the amphibolites have relatively low REE (4.26–30.62 ppm), LREE (3.06–19.19 ppm), and HREE (1.02–9.44 ppm) contents. The chondrite-normalized REE diagram for the amphibolite samples exhibits subparallel and slightly fractionated REE patterns [$(La/Yb)_N = 0.70$ –6.96] and significant Eu anomalies ($Eu/Eu^* = 0.82$ –2.09). These patterns lie below both the reference line for E-MORB [30] and the range reported for Dagele eclogites but overlap with gabbros from [12,22] (Figure 6a).

On a primitive mantle-normalized trace element spider diagram, the garnet amphibolites show enrichments in Th , U , Rb , Ta , and Pb and negative anomalies for Nb , Sr , and Eu . The overall patterns are distributed between the reference lines for E-MORB and OIB (Figure 6b). Additionally, the garnet amphibolite samples show 2–5 times higher contents of HREEs than the amphibolites, indicating that the dominant carrier of the HREEs is garnet (Figure 6b). The amphibolite samples have markedly negative anomalies in the HFSEs (e.g., Nb , Zr , Hf , and Th) and positive anomalies for the LILEs (e.g., Rb , Ba , Sr , and U), Eu , and Ta . Compared with the garnet amphibolite, this distinctly different pattern is likely due to the abundance of plagioclase in the amphibolites (Figure 6b).

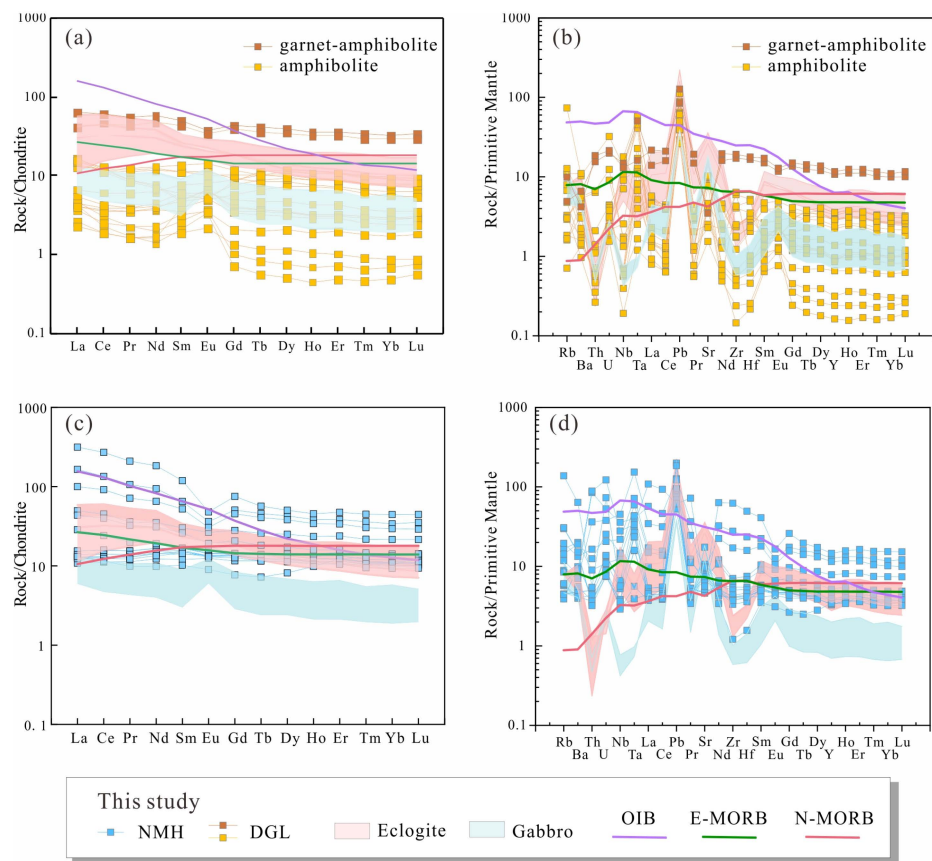


Figure 6. Chondrite-normalized REE patterns and primitive mantle-normalized trace element patterns for metabasites from (a,b) Dagele and (c,d) eastern Nuomuhong. Fields for eclogites and gabbros from Dagele area shown in figures are cited from the literature Du et al. [12]. Chondrite and primitive mantle values are from Sun and McDonough [30].

4.2.2. East Nuomuhong (NMH) Metabasites

Retrograde eclogites from east Nuomuhong have relatively low SiO₂ (43.19–50.15 wt.%, one sample with 58.86 wt.%), moderate variations in TiO₂ (0.427–2.608 wt.%), Al₂O₃ (13.75–19.01 wt.%), and alkalis (1.12–3.82 wt.%), and small variations in Mg# [41.07–60.11; atomic Mg/(Mg + Fe²⁺) × 100]. The samples lie in the basalt field on TAS (Figure 5a) and are characterized as basalts of the tholeiite series (Figure 5b–d).

Total REE contents range from 27–417 ppm, LREE's from 22–367 ppm, and HREE's from 10–51 ppm. On chondrite normalized diagrams, the samples show conspicuous negative Eu anomalies ($\delta\text{Eu} = 0.49\text{--}1.20$) and notable enrichments in LREEs (LaN/YbN = 1.09–4.86), similar to the patterns for E-MORB and OIB (Figure 6c). On primitive mantle-normalized diagrams, the samples show enrichments in U, Ta, and Pb and depletions in Sr, Nb, Zr, and Hf, roughly coinciding with the eclogites from [12] that have only minor plagioclase and abundant accessory minerals (Figure 6d).

4.3. Whole-Rock Sr–Nd Isotopes

The east Nuomuhong samples ($n = 10$) have an unusually wide range of initial Sr isotopic ratios (900 Ma) of 0.703352–0.747311 and positive ϵNd ($t = 900$ Ma) values of 1.88–5.64 (except for one sample with -1.53 ; Figure 7a–c; Table S6). Dagele samples ($n = 13$) have initial Sr isotopic ratios of 0.703216–0.709047 and a broader range in ϵNd ($t = 440$ Ma) values of -7.60 to $+5.10$ (Figure 7a–c; Table S6). Most samples overlap the OIB field on a diagram of $^{87}\text{Sr}/^{86}\text{Sr}$ vs. $^{143}\text{Nd}/^{144}\text{Nd}$ (Figure 7d; modified by [31]).

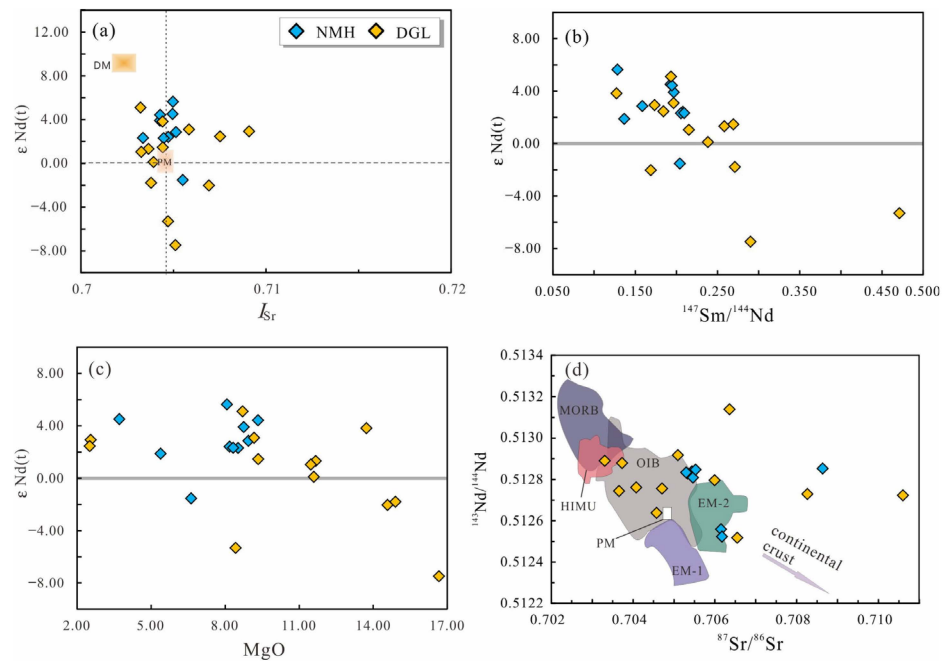


Figure 7. Sr-Nd isotope data for metabasites from Dagele [$\epsilon_{Nd}(t)$ and I_{Sr} calculated at 430 Ma] and east Nuomuhong [$\epsilon_{Nd}(t)$ and I_{Sr} calculated at 900 Ma]. (a) $\epsilon_{Nd}(t)$ vs. I_{Sr} . (b) $\epsilon_{Nd}(t)$ vs. $^{147}Sm/^{144}Nd$. (c) $\epsilon_{Nd}(t)$ vs. MgO. (d) $^{87}Sr/^{86}Sr$ vs. $^{143}Nd/^{144}Nd$, modified by Hofmann [31].

4.4. Phase Equilibrium Modeling

Pseudosection modeling for samples 20DGL97 and 20NMH81 was performed in the system NCKFMnMASHTO (Na_2O - CaO - K_2O - FeO - MnO - MgO - Al_2O_3 - SiO_2 - H_2O - TiO_2 - Fe_2O_3) using THERMOCALC 3.45 based on [32] with the internally consistent thermodynamic dataset ds62 [33]. Mixing models were used for melt, clinopyroxene and amphibole [34], garnet, orthopyroxene, mica and biotite [35], ilmenite [36], plagioclase [15], and epidote [33]. Pure phases included quartz, rutile, coesite, and aqueous fluid (H_2O). The bulk-rock compositions were taken from XRF analyses and normalized according to the NCKFMnMASHTO system (Table 1). The H_2O content for retrograde eclogite from east Nuomuhong (20NMH81) was determined by normalized calculation in efficient bulk-rock compositions so that the final phase assemblages are just stable above the solidus. The H_2O content of garnet amphibolite from Dagele (20DGL97) was set to excess due to the abundant hydrous minerals. Oxygen contents were determined according to mass balance constraints by adding the Fe^{3+} contents in each mineral calculated from the charge balance. All P_2O_5 was removed, and the total CaO was adjusted proportionally to account for the chemical contribution of apatite.

Table 1. Efficient bulk-rock compositions of metabasites from east Nuomuhong (sample 20NMH81) and Dagele (sample 20DGL97).

	20NMH81	20DGL97
H_2O	1.75	excess
SiO_2	49.45	54.96
Al_2O_3	10.39	8.28
CaO	10.84	10.15
MgO	13.37	3.35
TFeO	10.97	15.15
K_2O	0.05	0.06
Na_2O	2.15	1.93
TiO_2	1.13	2.33
MnO	0.13	0.23
O	0.22	0.84

The assemblage of symplectites of low-sodic clinopyroxene (below the 0.20 jadeite isopleth) + amphibole₂ + matrix plagioclase symplectites, which plots in the amphibole-bearing high-pressure granulite sub-facies (hb-HGR; M3) and is associated with consumption of M2 assemblage (garnet + omphacite). Pressure constraints from low-sodic clinopyroxene ($Jd(cpx) = 0.12\text{--}0.15$), together with a temperature estimate from X_{Ti} in amphibole (0.072–0.086 p.f.u.), define conditions of 10–12 kbar and 750–820 °C (peak temperature).

The M4 mineral assemblage features the appearance of orthopyroxene in low-sodic clinopyroxene + amphibole + plagioclase symplectites around the garnet, inferred to occur in the amphibole granulite sub-facies (hb-GR). The isopleths for $y(opx)$ (Al content in the M1 site of orthopyroxene) and $x(opx)$ ($Fe/(Fe + Mg)$) in the Grt + Cpx + Hb + Ru + Pl + Opx + Qtz field suggest a retrograde vector with decreasing T (~810 °C → ~750 °C → ~690 °C) and slightly decreasing P (9.5 → 8 kbar) from the amphibole-bearing HP granulite sub-facies into the granulite sub-facies (Figure 9b).

To model the P–T conditions of the final retrograde stage (M5), the inferred mineral assemblage (Grt, Cpx, Hb, Ilm, Pl, Opx ± Bi) was used in combination with the compositions of Amp-Pl-Ilm symplectites with the highest X_{An} values (0.61–0.63) and lowest $t(am)$ values (0.043–0.05). This indicates conditions of <7 kbar and <630 °C. Except for differences in accessory minerals (ilmenite occurs, rutile disappears), the inferred mineral assemblage in M5 is the same as in M4. However, the relevant mode isopleths reflect the growth of amphibole (26%–27%) and plagioclase (37%–38%) during M5 at the expense of clinopyroxene (6%–6.5%) and garnet (<5%) from M4. These constraints place the final retrograde amphibolite facies stage at 4.3–6.8 kbar and 590–630 °C (Figure 9b).

4.5. Zircon Geochronology and REE Patterns

4.5.1. Amphibolite from Dagele (20DGL99)

Cathodoluminescence (CL) images of representative zircons, as well as U–Pb ages and chondrite-normalized REE patterns, are shown in Figure 10. Zircons from Dagele amphibolites are subhedral to subrounded in shape, 200–400 µm in size, and have aspect ratios between 2 and 3 (Figure 10a). They contain distinct grey to dark-grey cores with oscillatory zoning and homogeneous grey to bright rims. Twenty-two analyses of zircon cores yielded a concordia age of 447.5 ± 1.7 Ma (MSWD = 1.5), slightly younger than the weighted-mean age of 448.7 ± 1.7 Ma (MSWD = 1.7; Tables S7 and S8). Seven analyses of rims yielded ages ranging from 421–405 Ma and a weighted mean age of 413.8 ± 3.7 Ma (MSWD = 6.6; Figure 10b). The cores and rims have similar REE patterns that are heavily enriched in HREE and show positive Ce anomalies and weakly negative Eu anomalies, consistent with the absence of garnet and only a minor amount of plagioclase (Figure 10c).

4.5.2. Garnet Amphibolite from Dagele (20DGL97)

Angular and euhedral zircons in garnet amphibolites are 100–150 µm long with aspect ratios of 1–2 (Figure 10d). In CL images, grains typically have dark cores and narrow, bright rims. One zircon with a homogenous fir-tree structure (upper right in Figure 10e) yielded an age of 421 ± 11 Ma. From a total of sixteen analyses of dark cores, five yielded relatively old ages of 531–488 Ma, while the other eleven yielded a concordant age of 438.6 ± 2.7 Ma (MSWD = 0.07), consistent with the weighted mean age of 440 ± 5 Ma (MSWD = 2.6; Figure 10e; Tables S7 and S8). Nine analyses conducted on the bright rims using 10 µm ablation spot dating [38], together with one analysis using a 33 µm ablation spot, yielded a nearly concordant age of 413.8 ± 1.4 Ma (MSWD = 2.2) and a weighted mean $^{206}Pb/^{238}U$ age of 414.2 ± 1.4 Ma (MSWD = 3.4).

Chondrite-normalized REE patterns of the dark cores showed a marked enrichment in HREE with negative Eu and positive Ce and Sm anomalies (Figure 10f; Table S9). The REE pattern of one metamorphic grain shows a flatter HREE pattern and a more subtle Eu anomaly compared to the cores.

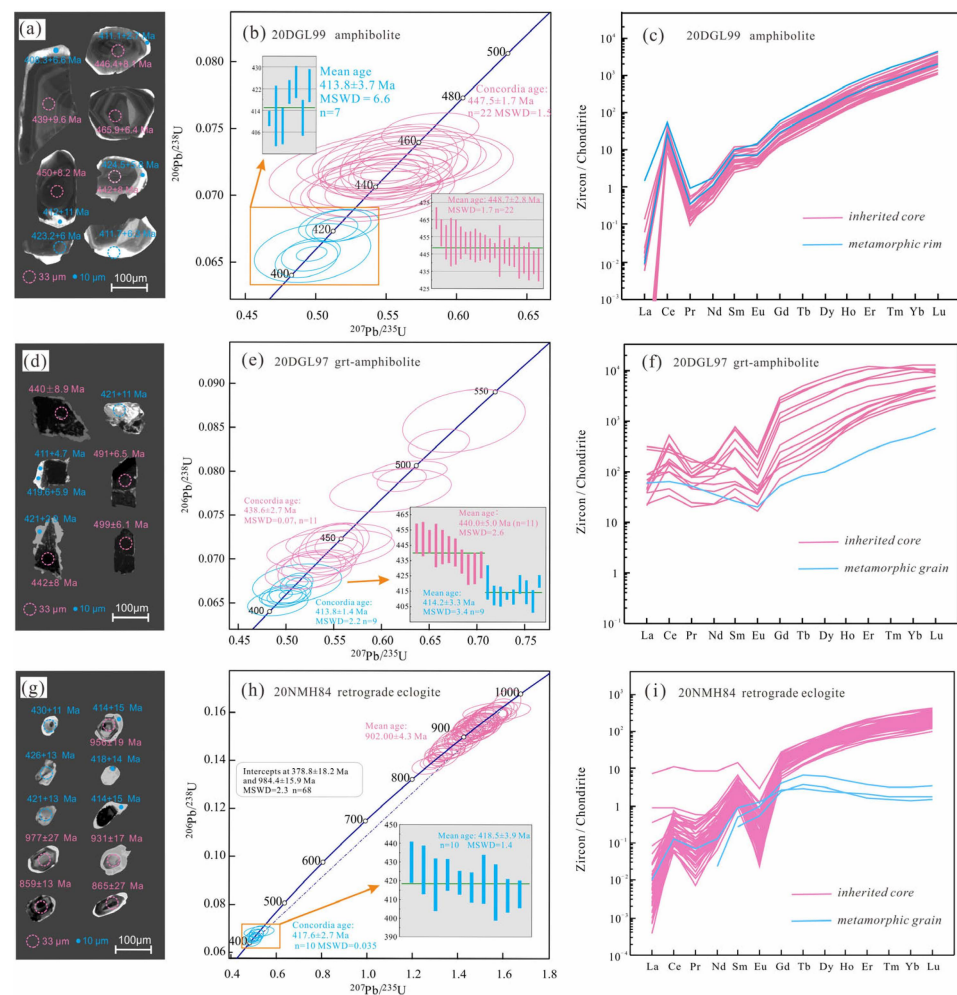


Figure 10. Cathodoluminescence (CL) images (**left column**), U-Pb concordia diagrams (**middle**) and chondrite-normalized REE patterns (**right**) of representative zircons from (**a–c**) Dagele amphibolites (20DGL99), (**d–f**) Dagele garnet amphibolites (20DGL97), and (**g–i**) east Nuomuhong retrograde eclogites (20NMH84). MSWD—mean square weighted deviation.

4.5.3. Retrograde Eclogite 20NMH84

Zircon grains in retrograde eclogite are mostly subhedral or elongated to prismatic shape and can be classified into two types. (1) Subrounded to subhedral grains are between 30–70 μm long and 30–50 μm wide, with aspect ratios between 1–1.5 (Figure 10g). These grains generally have homogenous dull luminescence, fir-tree structures, and low Th/U ratios (<0.1). (2) Subhedral to elongate prismatic grains are larger (70–100 μm) and have aspect ratios of 1–2.5. These grains show inherited dark grain cores with oscillatory zoning surrounded by narrow rims with lower luminescence.

The 68 analyses define a discordia with an upper intercept age of 984.4 ± 18.2 Ma and a lower intercept age of 378.8 ± 18.2 Ma (MSWD = 2.3). The 58 grain cores with oscillatory or simple zoning yield Precambrian ages ranging from 977–832 Ma, with a mean age of 902 Ma (Figure 10h). These have highly variable Th (1.7–25.4 ppm), U (7.2–146 ppm), and Th/U (0.11–1.31; Table S7). Ten analyses of the rims of grains (three with 33 μm spots and seven with 10 μm spots) yield a concordant or nearly concordant age of 417.6 ± 2.7 Ma (MSWD = 0.035) and an approximately equal-weighted mean age of 418.5 ± 3.9 Ma (MSWD = 1.4; Figure 10g; Table S8). The REE patterns for cores show a marked enrichment in HREEs and a prominent negative Eu anomaly. In comparison, rims show no Eu anomaly, lower HREE contents, and flat to depleted HREE patterns (Figure 10i; Table S9).

5. Discussion

5.1. Ages of Protoliths and Metamorphic Events

5.1.1. Dagele Amphibolite and Garnet Amphibolite

The zoned cores of zircons from amphibolite and garnet amphibolite yield similar weighted mean ages of, respectively, 448.7 Ma and 440 Ma, in good agreement with previous studies of Dagele gabbro ([12]; 445.9 ± 4.8 Ma), metabasites from Lalingzaohuo ([39]; 451 Ma), and basalt-diorite from Qimantagh ([40]; 443–446 Ma). This relatively tight spread of ages (451–440 Ma) suggests that the metabasites studied here belong to the same ophiolite mélange unit (QXM) as the previously studied samples. Additionally, the enrichment in HREE, negative Eu anomaly, and positive Ce and Sm anomalies, are similar to magmatic zircons summarized in [41], suggesting that the ages of the zircon cores represent the Late Ordovician to Early Silurian magmatic crystallization ages.

Analyses of luminescent zircon rims and fir-tree grains yielded younger ages of 413.8 ± 3.7 Ma and 414.2 ± 3.3 Ma, interpreted to represent Early Devonian metamorphic zircon growth. The REE patterns of zircon rims in amphibolite show no significant difference compared with magmatic cores, which may be due to the growth of amphibole during amphibolite facies metamorphism. Due to the fact that the REE pattern is mainly controlled by the characteristic elements partitioning between zircon and coexisting minerals, it is possible to infer coexisting mineral assemblages during various metamorphic phases based on the REE patterns. Thus, the eclogitic assemblages with garnet + albite breaking down to jadeite are coupled to an Eu-anomaly and flat HREE pattern and granulitic assemblage (feldspar + garnet) to a negative Eu-anomaly and flat HREE pattern. In regard to the 20DGL99 amphibolite in our study, the metamorphic assemblage of dominant amphibolite and a little feldspar without garnet is similar to the mineral composition of the protolith, and the amphibole could not lead to particularly obvious REE enrich or depleted characteristics. Therefore, the zircon from the protolith and metamorphic rock exhibit similar REE distribution characteristics of light-REE depletion and slight negative Eu-anomaly, which is also observed in amphibolite from previous studies [42]. This is consistent with the presence of amphibole and quartz inclusions in the rims of some zircons from sample 20DGL99. The REE pattern of one metamorphic grain in garnet amphibolites (Figure 10f) is compatible with zircon growth in a HREE-rich and Eu-bearing assemblage (e.g., garnet + amphibole + plagioclase) during upper-amphibolite facies metamorphism [41].

5.1.2. East Nuomuhong Retrograde Eclogite

Zircon cores yield Early Neoproterozoic $^{206}\text{Pb}/^{238}\text{U}$ ages, overlapping with tectono-thermal events (1.0–0.9 Ga) in the EKOB and North Qaidam. The cores show oscillatory zoning and have high Th/U ratios, steep HREE-enriched patterns, and marked negative Eu anomalies. On the basis of these characteristics [41], we suggest that the cores record Early Neoproterozoic magmatic crystallization to form the eclogite protoliths [19,43,44] rather than metamorphic events in the EKOB [45,46]. This is consistent with information retrieved from the Wenquan eclogite [11] and other Early Neoproterozoic magmatic rocks in East Kunlun [19,44]. Evidence of Neoproterozoic magmatism in the North Qaidam region has been widely interpreted in the context of the assembly of the Rodinia supercontinent, initially thought to reflect collision between the Tarim, Qaidam, and Qilian blocks [47,48]. More recently, the involvement of East Kunlun in the assembly of Rodinia has been proposed based on Neoproterozoic (1.0–0.9 Ma) ages for diverse tectono-thermal events recorded in this region [43–45]. Our new ages from zircon cores in retrograde eclogites from east Nuomuhong support the idea that East Kunlun was involved in the amalgamation of the Rodinia supercontinent.

Zircon rims and grains with homogenous dull luminescence yield a weighted mean age of 418.5 ± 3.9 Ma. These grains have subtle negative Eu anomalies, flat HREEs, low Th/U ratios, and garnet and omphacite as inclusions (Figure S1). Collectively, we interpret these data to represent the ages of eclogite facies metamorphism and zircon growth (Table S7). Previous studies have documented a relatively narrow age range of 433–425 Ma for eclogite facies

metamorphism in the EKOB and 410.5 ± 2 Ma for amphibolite facies metamorphism [8,10,12]. Based on our new results, we postulate that eclogite facies metamorphism may have persisted until c. 418 Ma, expanding the total duration of the eclogite facies metamorphic event to c. 17 Myr.

5.2. Nature of Mantle Protoliths

5.2.1. Assessment of Element Stability and Potential Crustal Contamination

The REEs and HFSEs are powerful tracers to identify basaltic (and metabasaltic) protoliths and tectonic affinities, even in samples that have experienced high-grade metamorphism or alteration by seawater. In the studied metabasites, the REEs (La, Nd, Yb) and HFSEs (Th, Y, Nb) display positive correlations with Zr (Figure S2), an immobile element that is widely used to analyze the effects of metamorphism and crustal contamination in eclogites. This suggests that La, Nd, Yb, Th, Y, Nb, and Zr in the studied metabasites exhibit similar behavior and remain immobile during high-grade metamorphism.

Determining the influence of crustal contamination on magma geochemistry is a fundamental step in determining the protolith characteristics. Three lines of isotopic and trace element evidence suggest that the metabasite protoliths experienced some, but limited, degrees of crustal contamination:

1. Relatively low La/Sm ratios in east Nuomuhong (1.39–4.09, avg. 2.12) and Dagele (1.06–5.31, avg. 2.29) compared with characteristics (La/Sm ratios > 4.5) of crustal contamination from [49];
2. Relatively low LILE oxide contents (e.g., K_2O , Na_2O and TiO_2);
3. The metabasites studied here have a narrower range of I_{Sr} compared with metabasites that experienced insignificant crustal contamination [50].

5.2.2. Primary Mantle Source

Negative correlations between MnO vs. MgO and TFe_2O_3 vs. MgO and a positive correlation between CaO vs. MgO (Figure S3) suggest that the metabasite protoliths underwent fractionation of olivine and clinopyroxene, consistent with the positive correlation between Ni and MgO (Figure S4).

Because of the different distribution coefficients between spinel and garnet, the element ratios of some REEs (e.g., La, Sm, Yb) and HFSEs (e.g., Zr, Nb, Y) are effective in tracing the degree of partial melting of basaltic source rocks in spinel- and garnet-bearing upper mantle. On a plot of La/Sm vs. Sm/Yb (Figure 11a), east Nuomuhong samples cluster into two groups: one representing spinel lherzolite with low degrees (~5%–10%) of partial melting and the second close to the curve for 10%–20% partial melting of lherzolite mantle with garnet < spinel. Dagele metabasites mainly plot close to the first group from east Nuomuhong, along the spinel lherzolite curve with low degrees (~5%–10%) of partial melting, but three samples represent very low degrees (<5%) of partial melting and two plot along a garnet lherzolite curve (Figure 11a).

Further modeling results using Sm vs. Sm/Yb (Figure 11b) show that the protoliths of east Nuomuhong metabasites were in the spinel or spinel + garnet fields [51], whereas the Dagele samples show a more widespread distribution. On a plot of Ce/Y vs. Zr/Nb (Figure 11c), which can be effective at distinguishing variations in source composition and degree of melting [52], metabasites from both areas mainly lie close to or between the primitive and depleted spinel lherzolite curves, indicating that protolith magmas were likely derived from a spinel lherzolite source with low degrees (1%–2%) of partial melting. Collectively, results suggest that the mantle sources of east Nuomuhong and Dagele samples were slightly different, which can be further assessed using the Ti/Yb vs. Nb/Yb plot from [53]. This shows that some Dagele samples plot above the MORB array and reach the OIB array (Figure 11d), indicating a higher temperature and deeper melting source for Dagele samples.

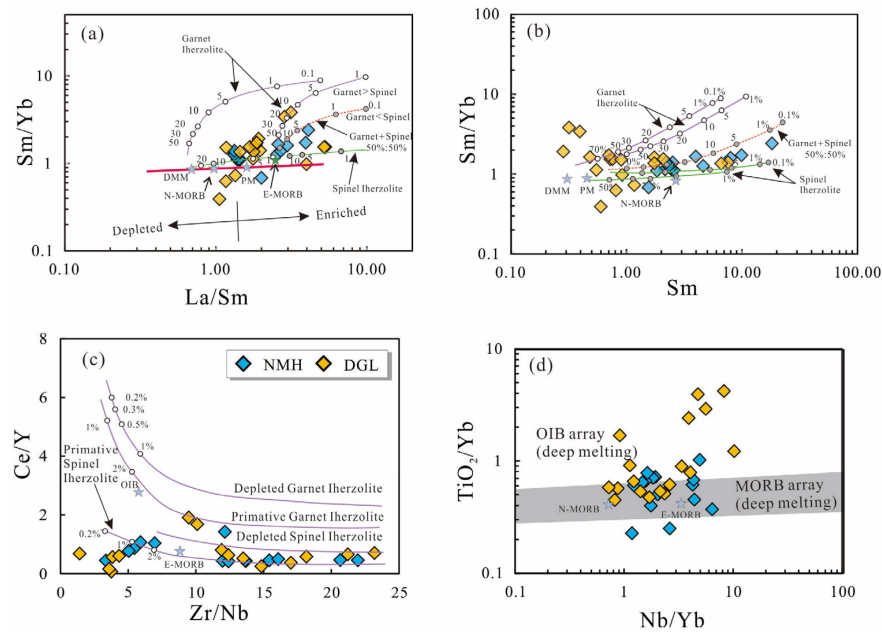


Figure 11. Plots of (a) Sm/Yb vs. La/Sm, (b) Sm vs. Sm/Yb, (c) Ce/Y vs. Zr/Nb, and (d) Ti/Yb vs. Nb/Yb for metabasites. Parts a–c show modeling results for partial melting in the garnet and spinel lherzolite stability fields. The N-MORB, E-MORB, and OIB data are from [30]. OIB—ocean island basalt; N-MORB—normal mid-oceanic ridge basalt; E-MORB—enriched mid-oceanic ridge basalt; PM—primitive mantle, and DMM—depleted MORB mantle.

5.2.3. Metasomatism of the Mantle Source and Discrimination of Protoliths

The primary geochemical characteristics of the mantle source may be modified by fluid or melt derived from subducted sediments [54], altered oceanic crust in the MORB section of the slab, or a complex mélange zone comprising sediment, oceanic crust, and serpentinite [55]. On the plot of Th vs. Ba/Th (Figure 12b), Dagele amphibolites also have relatively high Ba/Th ratios compared to garnet amphibolites and east Nuomuhong samples, suggesting that their protoliths were metasomatized by oceanic crust-derived aqueous fluids, while the garnet amphibolites and retrograde eclogites were metasomatized by sediment-derived melts [56]. This is supported by generally elevated Sr/Th ratios in the amphibolites—which likely reflects metasomatism of primary clinopyroxene by aqueous fluid [57] in a plot of Sr/Th vs. Th/Ce (Figure 12b). In contrast, the scatter of east Nuomuhong samples in Figure 12b is more compatible with metasomatism by a wet, sediment-derived siliceous melt [57].

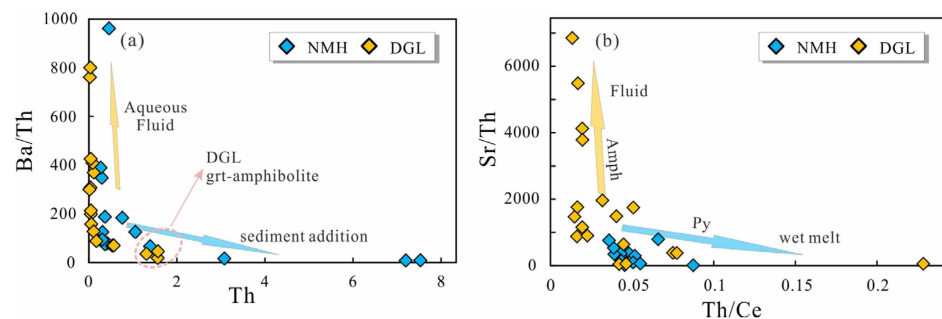


Figure 12. Plots of (a) Th vs. Ba/Th (b) Sr/Th vs. Th/Ce (Turner et al. [57]). Elevated Th/Ce is indicative of contributions from a sediment component but also a feature of the orthopyroxene in the xenoliths inferred to have been formed by metasomatism of pre-existing olivine by a wet, siliceous melt (Turner et al. [57]).

A new discrimination method of N-MORB normalized Nb and Th plotting (Saccani, E., 2015 [58]) has been applied in our study (Figure 13). The NMH metabasites are relatively concentrated and almost fall into the MORB region or overlap with back-arc basin basalt (BABB). The chemical variability of NMH metabasites, ranging from depleted compositions (N-MORB and G-MORB) to progressively more enriched compositions (E-MORB and P-MORB) and highly enriched compositions (AB), reflects the source composition and degree of melting. In contrast, the DGL metabasites are dispersed and mainly plotting in the island arc tholeiite (IAT), boninite and medium-Ti basalt (MTB), and Supra-subduction zone depleted MORB (SSZ-D-MORB) regions (Figure 13a), all these regions are related with arc setting.

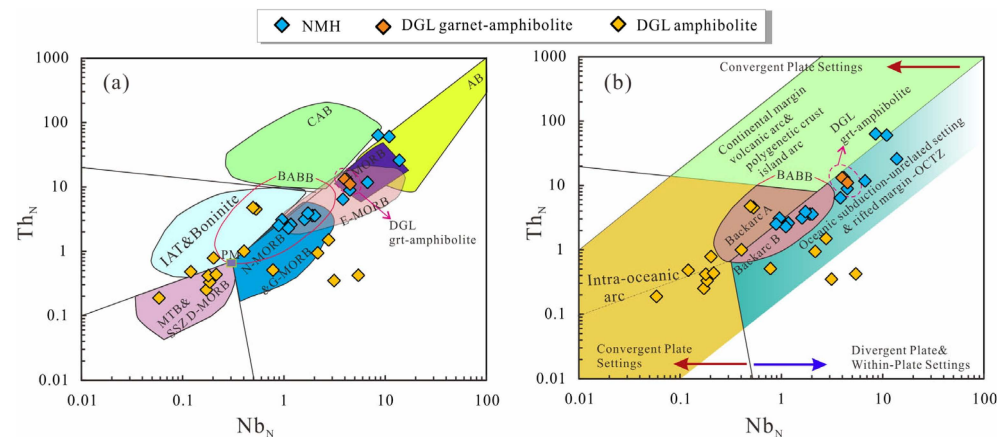


Figure 13. (a) Compositional variations of metabasite types on Th_N vs. Nb_N diagram. (b) Tectonic interpretation of metabasites based on Th_N vs. Nb_N systematics (modified by Saccani, E. [58]). Abbreviations: BABB—back-arc basin basalt; IAT—low-Ti, island arc tholeiite; CAB—calc-alkaline basalt; MTB—medium-Ti basalt; D-MORB—depleted-type basalt; SSZ-E—supra-subduction zone enrichment; AB—alkaline ocean-island basalt; G-MORB—garnet-influenced MORB; AFC—assimilation-fractional crystallization; OCTZ: ocean–continent transition zone. Backarc A indicates backarc basin basalts (BABB) characterized by input of subduction or crustal components (e.g., immature intra-oceanic or ensialic backarcs), whereas Backarc B indicates BABBs showing no input of subduction or crustal components (e.g., mature intra-oceanic backarcs). In both panels, Nb and Th are normalized to the N-MORB composition.

In the tectonic setting discrimination (Figure 13b), the NMH metabasites yield subduction-unrelated setting & rifted margin ranges, indicating the protoliths of NMH metabasites were continental setting basalts with Neoproterozoic age records. The DGL metabasites are related to arc settings, and the dispersed setting may be attributed to arc elemental variabilities accompanied with continuous arc magmatism during a variety of tectonic environments ranging from embryonic to mature back-arc and from oceanic to continental (ensialic) settings [59]. Notably, the DGL garnet-amphibolites plot in MORB type (Figure 13a) and show similar to these of subduction-unrelated setting (Figure 13b), general which is associated with the basaltic compositions from mature back-arcs [58]. In a review of the protolith age of garnet amphibolite 20DGL97, slightly younger than in amphibolite 20DGL99, it is suggested that the protolith of garnet amphibolite was generated in a more mature back-arc setting than amphibolite. Thus, the protoliths of DGL metabasites and NMH metabasites are back-arc basalts and within plate basalts, respectively.

5.3. Metamorphic Evolution and Tectonic Implications

On the basis of petrological observations, chemical analyses, zirconium-in-rutile thermometry, and phase equilibrium modeling, clockwise P–T paths were reconstructed for the metabasites from Dagele and east Nuomuhong (Figures 8 and 9). These are compared in

Figure 14 to other metabasites (eclogites, granulites, amphibolites) from the EKOB, which all show broadly clockwise P–T paths.

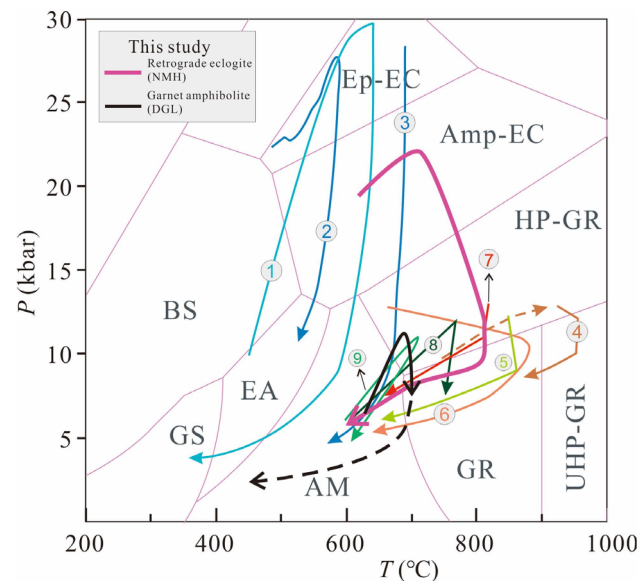


Figure 14. P–T paths of our samples and other metabasites (eclogites, granulites, amphibolites) from the EKOB. Published P–T paths: 1—eclogite from [8]; 2, 3—eclogite from [7]; 4—Qingshuiquan granulite from [60]; 5—Qingshuiquan granulite from [61]; 6—Qingshuiquan granulite from [62]; 7—Wulonggou HP granulite from [45]; 8—Adatan garnet amphibolite in Qiman Tagh from [63]; 9—Langmuri garnet amphibolite from [64]. Metamorphic facies after [65]. Abbreviations from [66].

Considering the geochemical interpretations discussed in Section 5.2, we infer that the basaltic protoliths to the Dagele metabasites formed in an oceanic basin setting where they experienced metasomatism by aqueous fluids derived from altered oceanic crust. The relatively short time gap between the formation (447–440 Ma) and metamorphic (414 Ma) ages recorded in the Dagele metabasites is consistent with results from other oceanic-derived metabasites [63,67] and may indicate that young oceanic crust was subducted shortly after it formed. However, the peak P–T conditions experienced by the garnet amphibolites from Dagele (Figure 14) restrict the depth of subduction to <40 km.

Blocks of retrograde eclogite in east Nuomuhong are found within granitic gneiss, suggesting that the eclogite protolith was emplaced into a continental setting [48,50]. This is consistent with geochemical results showing that metasomatism probably involved sediment-derived melts rather than fluids from the oceanic crust (Figure 12) and subduction-unrelated setting protolith characteristics (Figure 13). Furthermore, the significant time gap between the Neoproterozoic protolith age and Early Paleozoic metamorphism is also a common feature of continental-type metabasites (eclogites and granulites) from North Qaidam and Altyn Tagh [48,68]. Considering the geological and geochemical evidence, we interpret the protoliths of the retrograde eclogites to be continental tholeiitic basalts. The P–T conditions recorded by the retrograde eclogites (Figure 14) indicate that the basalts were subducted to depths of up to 70 km along a thermal gradient of ~11 °C/km (10–15 °C/km) during “hot plate” subduction [69].

Recent studies of the EKOB have emphasized the presence of two distinct ophiolite belts: a northern ophiolite belt that formed in the Early Paleozoic and a southern belt that formed discontinuously in the Early Paleozoic and Late Paleozoic [70]. The data on the two ophiolite belts have been synthesized, and the northern belt has the formation ages of 537–406 Ma [71]. However, other geologists advocated further subdivision of the northern ophiolite belt into the Qimantagh–Xiangride (QXM) and Aqikekulehu–Kunzhong (AKM) ophiolitic mélangé zones in [16]. Table 2 summarizes published age data and tectonic information on the QXM and AKM.

Table 2. Summary of published research on the QXM (light green) and AKM (gray).

Locality	Rock	Age	Tectonic Setting	Reference
Heishan	Mafic-ultramafic complex	486 Ma	Initial subduction of Qimantagh ocean basin in Early Ordovician	[2]
Heishan	Basalt	445 Ma	Subduction, back-arc spreading setting	[72]
Xarihamu	Gabbro	427 Ma	Continental subduction	
Yaziquan	Diorite	480 Ma	Intra-oceanic island arc	[2,73]
Shizigou	Gabbro	449 Ma	Small oceanic basin subduction	[74]
Changgou	Gabbro	431	Formation age of ophiolite	[75]
Yazidaban	Diabase	421.5 Ma	Subduction of the back-arc basin	[14]
Adatan	Garnet amphibolite	457–452 Ma 420–410 Ma	Subduction of the back-arc basin Continent collision	[63]
Dagele	Gabbro	445 Ma	Island arc environment of SSZ	[12]
Qingshui-quan	Granulite	507 Ma	Oceanic crust subduction	[61]
Qingshui-quan	Gabbro harzburgite	518 Ma -	SSZ forearc–arc setting	[6,76]
Changshi-shan	Gabbro	537 Ma	SSZ type	[77]
Qushi'ang	Meta-gabbro	505 Ma	SSZ back-arc basin	[5]
Acite	Meta-gabbro	512 Ma	Forearc–arc setting	[3]
Tatuo-Wutuo	Gabbro	522 Ma	SSZ back-arc basin	[78]
	Gabbro	516 Ma	SSZ slab rollback	[4]
Kekesha	Qtz-diorite	515 Ma	Start of oceanic basin subduction	[79]
Aqike kulehu	Peridotite-cumulate	-	Oceanic crust subduction	[80]

SSZ ophiolite—supra-subduction zone ophiolite.

It is clear from the data in Table 2 that the QXM (486–421 Ma) is significantly younger than the AKM (537–507 Ma), and thus the two ophiolitic mélangé zones likely represent two different tectonic sutures. With this in mind, we combine our results with previous studies to inform a new five-stage tectonic model for the evolution of East Kunlun in the Early Paleozoic, which emphasizes the role of “dominant” and “secondary” suture zones (Figure 15):

1. Stage I: Oceanic crust formation and initial subduction (>515 Ma)

The Proto-Tethys Ocean opened during the Neoproterozoic due to the breakup of Rodinia [81]. This overlaps with 1.0–0.9 Ga tectono-thermal events in Central Kunlun (Meng et al., 2013) and the crystallization ages of the eclogite protoliths in this study, confirming that the Central Kunlun Ocean represents an important branch of the Proto-Tethys. The ocean basin was well-established by 555 Ma (Figure 15; Ref. [82] supra-subduction zone type (SSZ-type) ophiolites along the AKM suggest that subduction of oceanic crust had initiated along a “dominant” suture boundary (predecessor of the Central Kunlun Fault) by the Early Cambrian (>537 Ma), consistent with metamorphic ages from the Qingshuiquan granulite, and amphibolite and gneiss (522–517 Ma) from southern Xiangride [60–62]. An age of 515 Ma obtained for the Kekesha quartz diorite has been interpreted to indicate ongoing subduction or even the cessation of subduction [79], bracketing the phase of seafloor spreading to c. 555–515 Ma.

2. Stage II: Small ocean basin formation (515–486 Ma)

Slab roll-back during continued subduction along the dominant suture boundary formed a series of small oceanic back-arc basins, including the Qimantagh and Adatan basins and the Dagele basin proposed here (Figure 15b). As the basins widened, the Central Kunlun Belt was formed from the original southern margin of the Qaidam Block. A SHRIMP age of 486 ± 6 Ma from a mafic–ultramafic complex in Heishan was interpreted to record subduction initiation in the Qimantagh Basin [2], suggesting that the small back-arc basins were mature no later than the Early Ordovician.

3. Stage III: Concurrent subduction along dominant and secondary suture boundaries (486 Ma to 427–421 Ma)

Subduction of the small basins along a secondary suture boundary (Figure 15c) is constrained by the ages of subduction-related basic rocks within the QXM [14,72]. In our study, the Dagele amphibolites and garnet amphibolites are interpreted to record the evolution of a small back-arc oceanic basin named the Dagele Ocean. The amphibolite protolith with a crystallization age of 447.5 Ma is interpreted to represent a gabbro intruded into the overlying gneissic crust during subduction of the Dagele Ocean. Similarly, the garnet-amphibolite protolith (crystallization age of 440 Ma) may represent arc-type magmatism. The metamorphic conditions and P–T path experienced by the garnet amphibolites are consistent with metamorphism at depths of 35–40 km in the thickened lower continental crust. Together with the metamorphic overprint (c. 414 Ma), this indicates that subduction of the Dagele Ocean may have persisted until c. 414 Ma and that upper amphibolite facies peak metamorphism may represent arc–continent collision between the Qaidam Block and the Central Kunlun Belt (Figure 15c). Therefore, we propose that (a) the newly identified metabasites in Dagele are part of the Qimantagh–Xiangride ophiolitic mélange zone (QXM), which formed within a secondary suture boundary, and (b) the model of “dominant” and “secondary” suture boundaries previously proposed for the Qimantagh area is also applicable to the Dagele area.

4. Stage IV: Subduction and collision along dominant and secondary suture zones (from 430–411 Ma)

Ongoing subduction of the Central Kunlun Ocean resulted in a collision between the South Kunlun Block and the Central Kunlun Belt along the dominant suture boundary (Figure 15d). This process is recorded by continental eclogites in the EKOB, including our samples from east Nuomuhong. By c. 430–411 Ma, the eclogites and metapelites had experienced UHP-HP metamorphism (Bi et al. [7]; Meng et al. [11]; this study) in response to continental subduction following the closure of the Central Kunlun Ocean. Granitic rocks in eastern Hongshuichuan record Middle Silurian partial melting of the thickened lower crust during continent–continent collision [75]. Additionally, other syn-collisional granites and post-collisional websterites along the Central Kunlun Fault formed during continental collisions between 432 and 408 Ma [83–86]. Thus, the Central Kunlun Ocean records a tectonic transition from subduction to continental collision between the Middle Silurian (c. 430 Ma) and Early Devonian (408 Ma).

5. Stage V: Post-collision extension and orogenic collapse (<411 Ma)

Delamination of the thickened lithosphere resulted in a change from compression to extension. This is recorded by post-collisional granitoids and mafic intrusions that collectively have an age range between 410 and 377 Ma in the Central Kunlun and North Qimantagh belts [84,85,87,88]. We suggest that Early- to Mid-Devonian heating from asthenospheric upwelling caused the amphibole–granulite sub-facies metamorphic overprint (hb-GR, M4) recorded in the retrograde eclogites studied here. Late Devonian molasse deposits [62,89] represent the terminal stages of post-orogenic collapse in East Kunlun (Figure 15e).

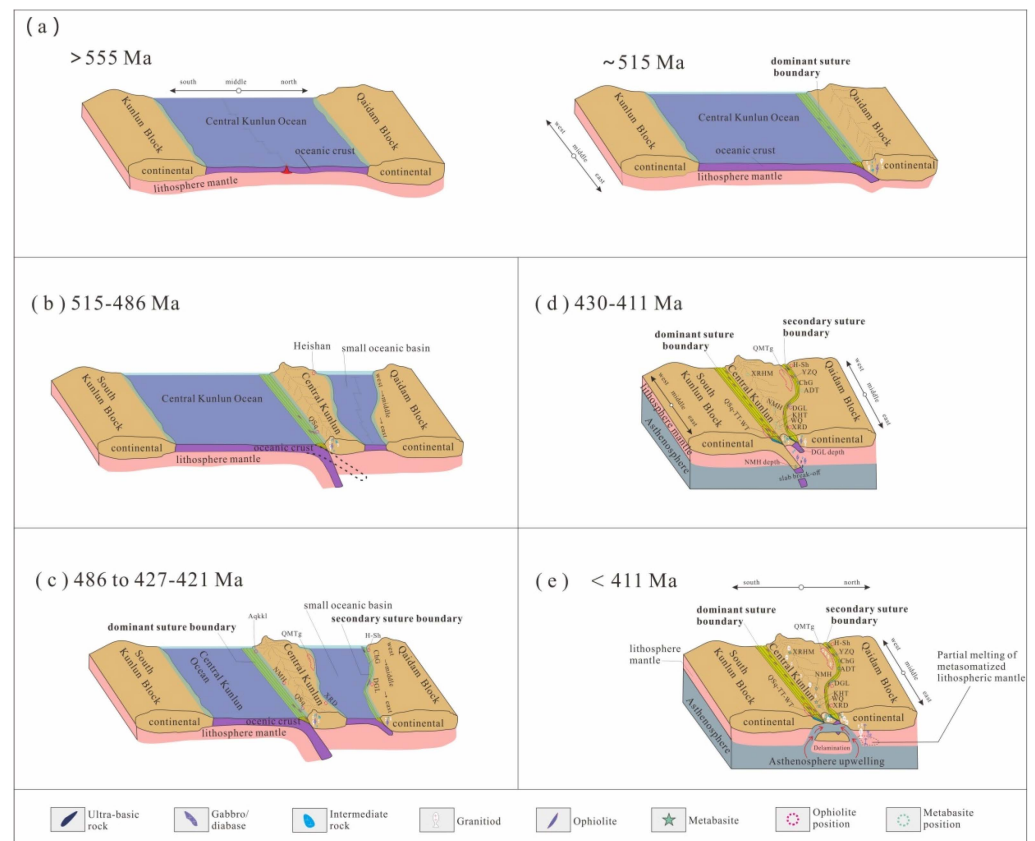


Figure 15. Inferred tectonic evolution of the Proto-Tethys Ocean and East Kunlun Orogenic Belt during the Early Palaeozoic. Aqkkl—Aqikekule, QSq-TT-WT—Quishuiquan–Tatuo–Wutuo; QMTg—Qiman–Tagh; H–Sh—Heishan; ChG—Changgou; YZQ—Yaziquan; ADT—Adatan; WQ—Wenquan; DGL—Dagele; NMH—Nuomuhong; KHT—Kehete; XRD—Xiangride; XRHM—Xiarhamu. Metabasites include retrograde eclogite, garnet amphibolite, and amphibolite.

6. Conclusions

We studied three types of metabasite from Dagele (amphibolite and garnet amphibolite) and east Nuomuhong (retrograde eclogite) in the central part of the East Kunlun Orogenic Belt. The protoliths of amphibolite and garnet amphibolite from Dagele formed at, respectively, c. 448.7 Ma (Late Ordovician) and c. 440 Ma (Early Silurian) and are interpreted to represent the products of arc-type magmatism related to the formation of the small Dagele back-arc basin. The garnet amphibolite records a clockwise P–T path, including Early Devonian (~414 Ma) peak amphibolite facies conditions of 11–12 kbar and 675–695 °C. The retrograde eclogite from east Nuomuhong yielded a Neoproterozoic protolith age of c. 902 Ma, interpreted to represent the intrusion of tholeiitic basalts into the lower continental crust. An Early Paleozoic eclogite facies (~21.5–22.2 kbar and 715–750 °C) metamorphic age of ~418 Ma extends the total duration of eclogite facies metamorphism in East Kunlun to 433–418 Ma. In our new tectonic model, retrograde eclogites from east Nuomuhong—together with other UHP–HP eclogites, metapelites, and ophiolites in the Aqikekulehu–Kunzhong ophiolitic mélangé zone (AKM)—record deep subduction between the Qaidam Block and the South Kunlun Block along a “dominant” suture boundary. By contrast, the newly identified Dagele metabasites associated with subduction–collision of the Dagele back-arc basin amalgamated with other ophiolitic suites from the Qimantagh–Xiangride ophiolitic mélangé zone (QXM) and eventually formed along a “secondary” suture boundary.

Supplementary Materials: The following supporting information can be downloaded at: <https://www.mdpi.com/article/10.3390/min14050449/s1>. Test S1: Analytical methods [90–95]; Figure S1: Raman spectra for omphacite and garnet inclusions in zircon; Figure S2: Plots of selected trace elements versus Zr for metabasites from the central part of East Kunlun, China; Figure S3: Plots of oxides versus MgO for metabasites from the central part of East Kunlun, China; Figure S4: Plots of Cr, Co, Ni, Nb versus MgO for metabasites from the central part of East Kunlun, China; Table S1: Representative garnet compositions for metabasites from the central East Kunlun Orogenic Belt; Table S2: Representative pyroxene compositions for metabasites from the central East Kunlun Orogenic Belt; Table S3: Representative amphibolite compositions for metabasites from the central East Kunlun Orogenic Belt; Table S4: Representative plagioclase compositions for metabasites from the central part of East Kunlun Orogenic Belt; Table S5: Whole-rock major and trace element compositions of metabasites (garnet amphibolite, amphibolite, and retrograde eclogite) from the central part of East Kunlun Orogenic Belt (EKOB); Table S6: Sr-Nd isotopes for metabasites from the central part of EKOB; Table S7: Zircon U-Pb ages by LA-ICP-MS (32 μm) for metabasites from the central part of EKOB; Table S8: Zircon U-Pb ages by LA-MC-ICP-MS (10 μm) for metabasites from the central part of EKOB; Table S9: Zircon trace-element compositions for metabasites from the central part of EKOB.

Author Contributions: Conceptualization, G.Z. and F.C.; methodology, G.Z. and S.L.; field survey and geological interpretation, G.Z. and F.C.; sample collection, G.Z., F.C., L.X. and S.L.; investigation and data processing, F.C.; writing—original draft preparation, F.C.; writing—review and editing G.Z., F.C. and S.L.; formal analysis, S.W. and Y.L.; supervision, G.Z., L.X. and S.L. All authors have read and agreed to the published version of the manuscript.

Funding: This research was funded by the National Natural Science Foundation of China (NSFC), grants 42372061, 41972056 and 91755206.

Data Availability Statement: All data can be provided from F.C. upon request due to the internal policy.

Acknowledgments: We are grateful to the editors and two anonymous reviewers for their constructive reviews and comments that substantially improved this work. We would like to thank Ying Cui and Xiaoli Li for their help with the experimental analysis. We are grateful to our driver, Jinbang He, who supported our group with fieldwork in Qinghai for over a decade.

Conflicts of Interest: The authors declare no conflicts of interest.

References

1. Zheng, Y.-F.; Chen, R.-X. Regional metamorphism at extreme conditions: Implications for orogeny at convergent plate margins. *J. Asian Earth Sci.* **2017**, *145*, 46–73. [[CrossRef](#)]
2. Meng, F.C.; Cui, M.H.; Wu, X.K.; Ren, Y.F. Heishan mafic–ultramafic rocks in the Qimantag area of Eastern Kunlun, NW China: Remnants of an early Paleozoic incipient island arc. *Gondwana Res.* **2015**, *27*, 745–759. [[CrossRef](#)]
3. Li, R.; Pei, X.; Li, Z.; Pei, L.; Chen, G.; Wei, B.; Chen, Y.; Liu, C.; Wang, M. Cambrian (~510 Ma) ophiolites of the East Kunlun orogen, China: A case study from the Acite ophiolitic tectonic mélange. *Int. Geol. Rev.* **2018**, *60*, 2063–2083. [[CrossRef](#)]
4. Li, R.; Pei, X.; Wei, B.; Li, Z.; Pei, L.; Chen, G.; Chen, Y.; Liu, C. Middle Cambrian–Early Ordovician ophiolites in the central fault of the East Kunlun Orogen: Implications for an epicontinental setting related to Proto-Tethyan Ocean subduction. *Gondwana Res.* **2021**, *94*, 243–258. [[CrossRef](#)]
5. Li, R.; Pei, X.; Wei, B.; Li, Z.; Pei, L.; Chen, Y.; Liu, C.; Cheng, G.; Wang, M.; Feng, K. Constraints of late Cambrian mafic rocks from the Qushi’ang ophiolite on a back-arc system in a continental margin, East Kunlun Orogen, Western China. *J. Asian Earth Sci.* **2019**, *169*, 117–129. [[CrossRef](#)]
6. Yang, J.S.; Robinson, P.T.; Jiang, C.F.; Xu, Z.Q. Ophiolites of the Kunlun Mountains, China and their tectonic implications. *Tectonophysics* **1996**, *258*, 215–231. [[CrossRef](#)]
7. Bi, H.; Whitney, D.L.; Song, S.; Zhou, X. HP–UHP eclogites in the East Kunlun Orogen, China: P–T evidence for asymmetric suturing of the Proto-Tethys Ocean. *Gondwana Res.* **2022**, *104*, 199–214. [[CrossRef](#)]
8. Song, S.G.; Bi, H.Z.; Qi, S.S.; Yang, L.M.; Allen, M.B.; Niu, Y.L.; Su, L.; Li, W.F. HP-UHP Metamorphic Belt in the East Kunlun Orogen: Final Closure of the Proto-Tethys Ocean and Formation of the Pan-North-China Continent. *J. Petrol.* **2018**, *59*, 2043–2060. [[CrossRef](#)]
9. Qi, S.S.; Song, S.G.; Shi, L.C.; Cai, H.J.; Hu, J.C. Discovery and its geological significance of Early Paleozoic eclogite in Xiarihamu-Suhaitu area, western part of the East Kunlun. *Acta Petrol. Sin.* **2014**, *11*, 3345–3356. (In Chinese with English abstract)
10. Qi, X.P.; Fan, X.G.; Yang, J.; Cui, J.T.; Wang, B.Y.; Fan, Y.Z. The discovery of Early Paleozoic eclogite in the upper reaches of Langmuri in eastern East Kunlun Mountains and its significance. *Geol. Bull. China* **2016**, *35*, 1771–1783. (In Chinese with English abstract)

11. Meng, F.; Zhang, J.; Cui, M. Discovery of Early Paleozoic eclogite from the East Kunlun, Western China and its tectonic significance. *Gondwana Res.* **2013**, *23*, 825–836. [[CrossRef](#)]
12. Du, W.; Jiang, C.; Xia, M.; Xia, Z.; Wei, Z.; Ling, J.; Wang, B. A newly discovered Early Paleozoic ophiolite in Dagele, Eastern Kunlun, China, and its geological significance. *Geol. J.* **2017**, *52*, 425–435. [[CrossRef](#)]
13. Zhou, W.; Chang, F.; Huang, B.; Xia, B.; Fu, D.; Chi Fru, E.; Li, H.; Lü, X.; Mao, C. Oceanic subduction to continental collision in the NE Proto-Tethys revealed by early Paleozoic eclogites with high-temperature granulite-facies overprinting in the East Kunlun orogenic belt, northern Tibet. *GSA Bull.* **2023**, *136*, 619–636. [[CrossRef](#)]
14. Dong, Y.; Sun, S.; Liu, X.; He, D.; Zhou, X.; Zhang, F.; Yang, Z.; Zhou, D. Geochronology and geochemistry of the Yazidaban ophiolitic mélangé in Qimantagh: Constraints on the Early Paleozoic back-arc basin of the East Kunlun Orogen, northern Tibetan Plateau. *J. Geol. Soc.* **2018**, *176*, 306–322. [[CrossRef](#)]
15. Holland, T.; Powell, R. Activity–composition relations for phases in petrological calculations: An asymmetric multicomponent formulation. *Contrib. Mineral. Petrol.* **2003**, *145*, 492–501. [[CrossRef](#)]
16. Dong, Y.; He, D.; Sun, S.; Liu, X.; Zhou, X.; Zhang, F.; Yang, Z.; Cheng, B.; Zhao, G.; Li, J. Subduction and accretionary tectonics of the East Kunlun orogen, western segment of the Central China Orogenic System. *Earth-Sci. Rev.* **2018**, *186*, 231–261. [[CrossRef](#)]
17. Feng, K.; Li, R.B.; Pei, X.Z.; Li, Z.C. Zircon U-Pb Dating and Geochemical Characteristics of Dagele Granite in the Eastern Margin of East Kunlun Orogenic Belt, China and Their Tectonic Implications. *J. Earth Sci. Environ.* **2020**, *42*, 442–463. (In Chinese with English abstract) [[CrossRef](#)]
18. Li, R.; Pei, X.; Li, Z.; Pei, L.; Chen, G.; Liu, Z.; Chen, Y.; Liu, C.; Wang, M.; Zhang, M. Paleo-Tethyan Ocean Evolution and Indosinian Orogenesis in the East Kunlun Orogen, Northern Tibetan Plateau. *Minerals* **2022**, *12*, 1590. [[CrossRef](#)]
19. He, D.; Dong, Y.; Liu, X.; Zhou, X.; Zhang, F.; Sun, S. Zircon U–Pb geochronology and Hf isotope of granitoids in East Kunlun: Implications for the Neoproterozoic magmatism of Qaidam Block, Northern Tibetan Plateau. *Precambrian Res.* **2018**, *314*, 377–393. [[CrossRef](#)]
20. Mo, X.X.; Luo, Z.H.; Deng, J.F.; Yu, X.H.; Liu, C.D.; Chen, H.W.; Liu, H.Y. Granitoids and Crustal Growth in the East Kunlun Orogenic Belt. *Geol. J. China Univ.* **2007**, *13*, 403–414. (In Chinese with English Abstract)
21. Dong, J.; Song, S.; Su, L.; Allen, M.B.; Li, Y.; Wang, C. Early Devonian mafic igneous rocks in the East Kunlun Orogen, NW China: Implications for the transition from the Proto- to Paleo-Tethys oceans. *Lithos* **2020**, 376–377, 105771. [[CrossRef](#)]
22. Morimoto, N. Nomenclature of pyroxenes. *Mineral. Petrol.* **1988**, *39*, 55–76. [[CrossRef](#)]
23. Smith, J.V. *Feldspar Minerals: In Three Volumes. 2. Chemical and Textural Properties*; Springer: Berlin/Heidelberg, Germany, 1974.
24. Leake, B.E.; Woolley, A.R.; Birch, W.D.; Burke, E.A.; Ferraris, G.; Grice, J.D.; Hawthorne, F.C.; Kisch, H.J.; Krivovichev, V.G.; Schumacher, J.C. Nomenclature of amphiboles: Additions and revisions to the International Mineralogical Association’s amphibole nomenclature. *Mineral. Mag.* **2004**, *68*, 209–215. [[CrossRef](#)]
25. Le Bas, M.J.; Le Maitre, R.W.; Streckeisen, A.; Zanettin, B. A Chemical Classification of Volcanic Rocks Based on the Total Alkali-Silica Diagram. *J. Petrol.* **1986**, *27*, 745–750. [[CrossRef](#)]
26. Irvine, T.N.; Baragar, W.R.A. A Guide to the Chemical Classification of the Common Volcanic Rocks. *Can. J. Earth Sci.* **1971**, *8*, 523–548. [[CrossRef](#)]
27. Pearce, J.A.; Peate, D.W. Tectonic Implications of the Composition of Volcanic ARC Magmas. *Annu. Rev. Earth Planet. Sci.* **1995**, *23*, 251–285. [[CrossRef](#)]
28. Sengun, F. Geochemistry and Tectonic Setting of Amphibolites in the Pamukova Metamorphics from the Armutlu Peninsula, NW Turkey. *Arab. J. Geosci.* **2022**, *15*, 605. [[CrossRef](#)]
29. Hastie, A.R.; Kerr, A.C.; Pearce, J.A.; Mitchell, S.F. Classification of Altered Volcanic Island Arc Rocks using Immobile Trace Elements: Development of the Th–Co Discrimination Diagram. *J. Petrol.* **2007**, *48*, 2341–2357. [[CrossRef](#)]
30. Sun, S.S.; McDonough, W.F. *Chemical and Isotopic Systematic of Oceanic Basalt: Implications for the Mantle Composition and Processes*; Special Publications; Geological Society: London, UK, 1989; Volume 42, pp. 313–345.
31. Hofmann, A.W. Mantle geochemistry: The message from oceanic volcanism. *Nature* **1997**, *385*, 219–229. [[CrossRef](#)]
32. Powell, R.; Holland, T.; Worley, B. Calculating phase diagrams involving solid solutions via non-linear equations, with examples using THERMOCALC. *J. Metamorph. Geol.* **1998**, *16*, 577–588. [[CrossRef](#)]
33. Holland, T.J.B.; Powell, R. An improved and extended internally consistent thermodynamic dataset for phases of petrological interest, involving a new equation of state for solids. *J. Metamorph. Geol.* **2011**, *29*, 333–383. [[CrossRef](#)]
34. Green, E.C.R.; White, R.W.; Diener, J.F.A.; Powell, R.; Holland, T.J.B.; Palin, R.M. Activity–composition relations for the calculation of partial melting equilibria in metabasic rocks. *J. Metamorph. Geol.* **2016**, *34*, 845–869. [[CrossRef](#)]
35. White, R.W.; Powell, R.; Holland, T.J.B.; Johnson, T.E.; Green, E.C.R. New mineral activity–composition relations for thermodynamic calculations in metapelitic systems. *J. Metamorph. Geol.* **2014**, *32*, 261–286. [[CrossRef](#)]
36. White, R.W.; Powell, R.; Holland, T.J.B.; Worley, B.A. The effect of TiO₂ and Fe₂O₃ on metapelitic assemblages at greenschist and amphibolite facies conditions: Mineral equilibria calculations in the system K₂O–FeO–MgO–Al₂O₃–SiO₂–H₂O–TiO₂–Fe₂O₃. *J. Metamorph. Geol.* **2000**, *18*, 497–511. [[CrossRef](#)]
37. Tomkins, H.S.; Powell, R.; Ellis, D.J. The pressure dependence of the zirconium-in-rutile thermometer. *J. Metamorph. Geol.* **2007**, *25*, 703–713. [[CrossRef](#)]
38. Lin, M.; Zhang, G.; Li, N.; Li, H.; Wang, J. An Improved In Situ Zircon U-Pb Dating Method at High Spatial Resolution ($\leq 10 \mu\text{m}$ Spot) by LA-MC-ICP-MS and its Application. *Geostand. Geoanalytical Res.* **2021**, *45*, 265–285. [[CrossRef](#)]

39. Wang, P.; Guo, F.; Wang, Z.; Feng, N. Zircon U-Pb Chronology, Geological and Geochemical Characteristics of Metamorphosed Basic Rocks in the Middle Reaches of Lalingzaohuo, Qimantage Area of East Kunlun Mountains. *Can. J. Earth Sci.* **2021**, *27*, 408–421. [[CrossRef](#)]
40. Li, W.; Neubauer, F.; Liu, Y.; Genser, J.; Ren, S.; Han, G.; Liang, C. Paleozoic evolution of the Qimantagh magmatic arcs, Eastern Kunlun Mountains: Constraints from zircon dating of granitoids and modern river sands. *J. Asian Earth Sci.* **2013**, *77*, 183–202. [[CrossRef](#)]
41. Rubatto, D. Zircon: The Metamorphic Mineral. *Rev. Mineral. Geochem.* **2017**, *83*, 261–295. [[CrossRef](#)]
42. Rubatto, D.; Hermann, J.; Berger, A.; Engi, M. Protracted fluid-induced melting during Barrovian metamorphism in the Central Alps. *Contrib. Mineral. Petrol.* **2009**, *158*, 703–722. [[CrossRef](#)]
43. Jian, X.; Weislogel, A.; Pullen, A.; Shang, F. Formation and evolution of the Eastern Kunlun Range, northern Tibet: Evidence from detrital zircon U-Pb geochronology and Hf isotopes. *Gondwana Res.* **2020**, *83*, 63–79. [[CrossRef](#)]
44. Tang, H.; Zhang, H.F.; Zhang, M.J.; Zou, H.; Zhang, J. Neoproterozoic and early Paleozoic metamorphism recorded in gneisses from the East Kunlun Orogenic belt. *Precambrian Res.* **2022**, *375*, 106650. [[CrossRef](#)]
45. He, D.; Dong, Y.; Hauzenberger, C.A.; Sun, S.; Neubauer, F.; Zhou, B.; Yue, Y.; Hui, B.; Ren, X.; Chong, F. Neoproterozoic HP granulite and its tectonic implication for the East Kunlun Orogen, northern Tibetan Plateau. *Precambrian Res.* **2022**, *378*, 106–778. [[CrossRef](#)]
46. He, D.; Dong, Y.; Liu, X.; Yang, Z.; Sun, S.; Cheng, B.; Li, W. Tectono-thermal events in East Kunlun, Northern Tibetan Plateau: Evidence from zircon U-Pb geochronology. *Gondwana Res.* **2016**, *30*, 179–190. [[CrossRef](#)]
47. Lu, S.; Li, H.; Zhang, C.; Niu, G. Geological and geochronological evidence for the Precambrian evolution of the Tarim Craton and surrounding continental fragments. *Precambrian Res.* **2008**, *160*, 94–107. [[CrossRef](#)]
48. Song, S.; Niu, Y.; Su, L.; Zhang, C.; Zhang, L. Continental orogenesis from ocean subduction, continent collision/subduction, to orogen collapse, and orogen recycling: The example of the North Qaidam UHPM belt, NW China. *Earth-Sci. Rev.* **2014**, *129*, 59–84. [[CrossRef](#)]
49. Lassiter, J.C.; DePaolo, D.J. Plume/Lithosphere Interaction in the Generation of Continental and Oceanic Flood Basalts: Chemical and Isotopic Constraints. In *Large Igneous Provinces: Continental, Oceanic, and Planetary Flood Volcanism*; Lassiter, J.C., DePaolo, D.J., Eds.; Wiley: Hoboken, NJ, USA, 1997; pp. 335–355.
50. Zhang, G.; Wang, J.; Webb, A.A.G.; Zhang, L.; Liu, S.; Fu, B.; Wu, C.; Wang, S. The protoliths of central Himalayan eclogites. *GSA Bull.* **2021**, *134*, 1949–1966. [[CrossRef](#)]
51. Aldanmaz, E.; Pearce, J.A.; Thirlwall, M.F.; Mitchell, J.G. Petrogenetic evolution of late Cenozoic, post-collision volcanism in western Anatolia, Turkey. *J. Volcanol. Geotherm. Res.* **2000**, *102*, 67–95. [[CrossRef](#)]
52. Deniel, C. Geochemical and isotopic (Sr, Nd, Pb) evidence for plume–lithosphere interactions in the genesis of Grande Comore magmas (Indian Ocean). *Chem. Geol.* **1998**, *144*, 281–303. [[CrossRef](#)]
53. Pearce, J.A. Geochemical fingerprinting of oceanic basalts with applications to ophiolite classification and the search for Archean oceanic crust. *Lithos* **2008**, *100*, 14–48. [[CrossRef](#)]
54. Class, C.; Miller, D.M.; Goldstein, S.L.; Langmuir, C.H. Distinguishing melt and fluid subduction components in Umnak Volcanics, Aleutian Arc. *Geochem. Geophys. Geosyst.* **2000**, *1*, 10. [[CrossRef](#)]
55. Li, H.; Hermann, J.; Zhang, L. Melting of subducted slab dictates trace element recycling in global arcs. *Sci. Adv.* **2022**, *8*, eab2166. [[CrossRef](#)] [[PubMed](#)]
56. Furnes, H.; Dilek, Y. Geochemical characterization and petrogenesis of intermediate to silicic rocks in ophiolites: A global synthesis. *Earth-Sci. Rev.* **2017**, *166*, 1–37. [[CrossRef](#)]
57. Turner, S.; Caulfield, J.; Turner, M.; van Keken, P.; Maury, R.; Sandiford, M.; Prouteau, G. Recent contribution of sediments and fluids to the mantle’s volatile budget. *Nat. Geosci.* **2012**, *5*, 50–54. [[CrossRef](#)]
58. Saccani, E. A new method of discriminating different types of post-Archean ophiolitic basalts and their tectonic significance using Th-Nb and Ce-Dy-Yb systematics. *Geosci. Front.* **2015**, *6*, 481–501. [[CrossRef](#)]
59. Dilek, Y.; Furnes, H. Ophiolite genesis and global tectonics: Geochemical and tectonic fingerprinting of ancient oceanic lithosphere. *GSA Bull.* **2011**, *123*, 387–411. [[CrossRef](#)]
60. Bi, H.; Song, S.; Whitney, D.L.; Wang, C.; Su, L. HP–UHT granulites in the East Kunlun Orogen, NW China: Constraints on the transition from compression to extension in an arc setting of the Proto-Tethys Ocean. *J. Metamorph. Geol.* **2021**, *39*, 1071–1095. [[CrossRef](#)]
61. He, D.; Dong, Y.; Hauzenberger, C.A.; Sun, S.; Liu, X.; Yue, Y. Pressure-temperature evolution of the Qingshuiquan mafic granulite: Implications for Proto-Tethys subduction in the East Kunlun orogenic belt, northern Tibetan Plateau. *GSA Bull.* **2022**, *135*, 1034–1052. [[CrossRef](#)]
62. Chen, N.; Sun, M.; Wang, Q.; Zhang, K.; Wan, Y.; Chen, H. U-Pb dating of zircon from the Central Zone of the East Kunlun Orogen and its implications for tectonic evolution. *Sci. China Ser. D Earth Sci.* **2008**, *51*, 929–938. [[CrossRef](#)]
63. Zha, X.; Dong, Y.; He, D.; Li, M.; Gao, X.; Liu, X.; Hu, C.; Xu, L. Early palaeozoic arc-continent collision in East Kunlun, northern Tibet: Evidence from the mineralogy, geochemistry, and geochronology of the Adatan garnet amphibolites. *Int. Geol. Rev.* **2022**, *65*, 1–21. [[CrossRef](#)]
64. Li, C.; Zhang, H.F.; Chen, A. Early Paleozoic metamorphic evolution of the East Kunlun Orogen recorded in Langmuri garnet-amphibolite. *Acta Petrol. Sin.* **2022**, *38*, 639–654. (In Chinese with English abstract)

65. Maruyama, S.; Liou, J.G. Initiation of ultrahigh-pressure metamorphism and its significance on the Proterozoic–Phanerozoic boundary. *Isl. Arc* **1998**, *7*, 6–35. [[CrossRef](#)]
66. Whitney, D.L.; Evans, B.W. Abbreviations for names of rock-forming minerals. *Am. Mineral.* **2010**, *95*, 185–187. [[CrossRef](#)]
67. Zhang, G.; Han, L.; Zhang, L.; Song, S.; Liu, S. The transition from oceanic to continental subduction and collision: A case study of the North Qaidam ultrahigh-pressure metamorphic belt, northern Tibetan Plateau. *J. Asian Earth Sci.* **2023**, *242*, 105488. [[CrossRef](#)]
68. Dong, J.; Wei, C.J.; Zhang, J.X. Ultra high temperature metamorphism of mafic granulites from South Altyn Orogen, West China: A result from the rapid exhumation of deeply subducted continental crust. *J. Metamorph. Geol.* **2018**, *3*, 315–338. [[CrossRef](#)]
69. Zhang, Z.; Ding, H.; Dong, X.; Tian, Z.; Du, J. Metamorphism and tectonic mechanisms of subduction zones. *Acta Petrol. Sin.* **2021**, *37*, 3377–3398. (In Chinese with English abstract) [[CrossRef](#)]
70. Wu, F.; Wan, B.; Zhao, L.; Xiao, W.; Zhu, R. Tethyan geodynamics. *Acta Petrol. Sin.* **2020**, *36*, 1627–1674. (In Chinese with English abstract)
71. Wen, T.; Dong, J.; Wang, C.; Song, S. Two ophiolite belts in the East Kunlun Orogenic Belt record evolution from the Proto-Tethys to Paleo-Tethys Oceans. *Int. Geol. Rev.* **2022**, *65*, 1957–1976. [[CrossRef](#)]
72. Duan, X.-P.; Meng, F.-C.; Jia, L.-H. Early Paleozoic mantle evolution of East Kunlun Orogenic Belt in Qinghai, NW China: Evidence from the geochemistry and geochronology of the Late Ordovician to Late Silurian mafic-ultramafic rocks in the Qimantag region. *Int. Geol. Rev.* **2020**, *62*, 1883–1903. [[CrossRef](#)]
73. Cui, M.H.; Meng, F.C.; Wu, X.K. Early Ordovician island arc of Yaziquan, west of Qimantag Mountain, East Kunlun: Evidences from geochemistry, Sm-Nd isotope and geochronology of intermediate-basic rocks. *Acta Petrol. Sin.* **2011**, *27*, 3365–3379. (In Chinese with English abstract)
74. Song, T.Z.; Zhao, H.X.; Zhang, W.K.; Bai, X.D.; Yang, M. The Geological Features of Shizigou Ophiolites in Qimantag Area. *Northwestern Geol.* **2010**, *43*, 124–133. (In Chinese with English abstract)
75. Dong, G.; Luo, M.; Mo, X.; Zhao, Z.; Dong, L.; Yu, X.; Wang, X.; Li, X.; Huang, X.; Liu, Y. Petrogenesis and tectonic implications of early Paleozoic granitoids in East Kunlun belt: Evidences from geochronology, geochemistry and isotopes. *Geosci. Front.* **2018**, *9*, 1383–1397. [[CrossRef](#)]
76. Feng, H.B.; Meng, F.C.; Li, S.R.; Jia, L.H. Characteristics and tectonic significance of chromites from Qingshuiquan serpentinite of East Kunlun, Northwest China. *Acta Petrol. Sin.* **2015**, *31*, 2129–2144. (In Chinese with English abstract)
77. Qi, X.P.; Yang, J.; Fan, X.G.; Cui, J.T.; Cai, Z.F.; Zeng, X.W.; Wei, W.; Qu, X.X.; Zhai, Y.M. Age, geochemical characteristics and tectonic significance of Changshishan ophiolite in central East Kunlun tectonic mélange belt along the east section of East Kunlun Mountains. *Geol. China* **2016**, *43*, 797–816. [[CrossRef](#)]
78. Wei, B. Study on the Geological Characteristic and Tectonic Attribute of the Ophiolite and Island-Arc-Type Igneous Rocks, Central Belt of East Kunlun (Eastern Section). Master's Thesis, Chang'an University, Xi'an, China, 2015.
79. Zhang, Y.; Pei, X.; Ding, S.; Li, R.; Feng, J.; Sun, Y.; Li, Z.; Chen, Y. LA-ICP-MS zircon U-Pb age of quartz diorite at the Kekesha area of Dulan County, eastern section of the East Kunlun orogenic belt, China and its significance. *Geol. Bull. China Geol.* **2010**, *29*, 79–85.
80. Wu, J.; Lan, C.L.; Li, J.L.; Yu, L.J. Determination of ophiolite at the western margin of Aqikekule lake, east Kunlun of Xijiang. *Geol. Sci. Technol. Inf.* **2001**, *20*, 6–10.
81. Li, S.; Zhao, S.; Liu, X.; Cao, H.; Yu, S.; Li, X.; Somerville, I.; Yu, S.; Suo, Y. Closure of the Proto-Tethys Ocean and Early Paleozoic amalgamation of microcontinental blocks in East Asia. *Earth-Sci. Rev.* **2018**, *186*, 37–75. [[CrossRef](#)]
82. Li, R.; Pei, X.; Li, Z.; Sun, Y.; Feng, J.; Pei, L.; Chen, G.; Liu, C.; Chen, Y. Geochemical Features, Age, and Tectonic Significance of the Kekekete Mafic-ultramafic Rocks, East Kunlun Orogen, China. *Acta Geol. Sin. Engl. Ed.* **2013**, *87*, 1319–1333. [[CrossRef](#)]
83. Chen, J.; Fu, L.; Wei, J.; Selby, D.; Zhang, D.; Zhou, H.; Zhao, X.; Liu, Y. Proto-Tethys magmatic evolution along northern Gondwana: Insights from Late Silurian–Middle Devonian A-type magmatism, East Kunlun Orogen, Northern Tibetan Plateau, China. *Lithos* **2020**, *356–357*, 105304. [[CrossRef](#)]
84. Song, X.-Y.; Yi, J.-N.; Chen, L.-M.; She, Y.-W.; Liu, C.-Z.; Dang, X.-Y.; Yang, Q.-A.; Wu, S.-K. The Giant Xiarihamu Ni-Co Sulfide Deposit in the East Kunlun Orogenic Belt, Northern Tibet Plateau, China. *Econ. Geol.* **2016**, *111*, 29–55. [[CrossRef](#)]
85. Xin, W.; Sun, F.-Y.; Li, L.; Yan, J.-M.; Zhang, Y.-T.; Wang, Y.-C.; Shen, T.-S.; Yang, Y.-J. The Wulonggou metaluminous A2-type granites in the Eastern Kunlun Orogenic Belt, NW China: Rejuvenation of subduction-related felsic crust and implications for post-collision extension. *Lithos* **2018**, *312–313*, 108–127. [[CrossRef](#)]
86. Zhang, J.; Ma, C.; Xiong, F.; Liu, B.; Li, J.; Pan, Y. Early Paleozoic high-Mg diorite-granodiorite in the eastern Kunlun Orogen, western China: Response to continental collision and slab break-off. *Lithos* **2014**, *210–211*, 129–146. [[CrossRef](#)]
87. Zhang, J.; Lei, H.; Ma, C.; Li, J.; Pan, Y. Silurian-Devonian granites and associated intermediate-mafic rocks along the eastern Kunlun Orogen, western China: Evidence for a prolonged post-collisional lithospheric extension. *Gondwana Res.* **2021**, *89*, 131–146. [[CrossRef](#)]
88. Fu, L.; Bagas, L.; Wei, J.; Chen, Y.; Chen, J.; Zhao, X.; Zhao, Z.; Li, A.; Zhang, W. Growth of early Paleozoic continental crust linked to the Proto-Tethys subduction and continental collision in the East Kunlun Orogen, northern Tibetan Plateau. *GSA Bull.* **2022**, *135*, 1709–1733. [[CrossRef](#)]
89. Yu, M.; Dick, J.M.; Feng, C.; Li, B.; Wang, H. The tectonic evolution of the East Kunlun Orogen, northern Tibetan Plateau: A critical review with an integrated geodynamic model. *J. Asian Earth Sci.* **2020**, *191*, 104168. [[CrossRef](#)]

90. Cui, H.; Zhong, R.; Wang, X.; Li, Z.; Ling, Y.; Yu, C.; Chen, H. Reassessment of the zircon Raman spectroscopic pressure sensor and application to pressure determination of fused silica capillary capsule. *Ore Geol. Rev.* **2020**, *122*, 103540. [[CrossRef](#)]
91. Li, C.-F.; Li, X.-H.; Li, Q.-L.; Guo, J.-H.; Li, X.-H.; Yang, Y.-H. Rapid and precise determination of Sr and Nd isotopic ratios in geological samples from the same filament loading by thermal ionization mass spectrometry employing a single-step separation scheme. *Anal. Chim. Acta* **2012**, *727*, 54–60. [[CrossRef](#)]
92. Li, X.; Zhang, L.; Wei, C.; Slabunov, A.I.; Bader, T. Quartz and orthopyroxene exsolution lamellae in clinopyroxene and the metamorphic P - T path of Belomorian eclogites. *J. Metamorph. Geol.* **2017**, *36*, 1–22. [[CrossRef](#)]
93. Vermeesch, P. IsoplotR: A free and open toolbox for geochronology. *Geosci. Front.* **2018**, *9*, 1479–1493. [[CrossRef](#)]
94. Wiedenbeck, M.; Allé, P.; Corfu, F.; Griffin, W.L.; Meier, M.; Oberli, F.; Quadt, A.V.; Roddick, J.C.; Spiegel, W. Three Natural Zircon Standards for U-Th-Pb, Lu-Hf, Trace Element and REE Analyses. *Geostand. Newsl.* **1995**, *19*, 1–23. [[CrossRef](#)]
95. Xiong, L.; Zhang, G.; Song, S.; Liu, S.; Feng, D.; Chang, F. Eclogite in the East Kunlun Orogen, northwestern China: A record of the Neoproterozoic breakup of Rodinia and early Paleozoic continental subduction. *GSA Bull.* **2023**. [[CrossRef](#)]

Disclaimer/Publisher’s Note: The statements, opinions and data contained in all publications are solely those of the individual author(s) and contributor(s) and not of MDPI and/or the editor(s). MDPI and/or the editor(s) disclaim responsibility for any injury to people or property resulting from any ideas, methods, instructions or products referred to in the content.